Momentum transfer during the impact of granular matter with inclined sliding surfaces

Anne Kyner, Vikram Deshpande* and Haydn Wadley

Department of Materials Science and Engineering, University of Virginia, Charlottesville, Va 22903, USA

* Engineering Department, Cambridge University, UK

Abstract

Increasing the inclination of a rigid surface that is impacted by a collimated granular flow reduces the fraction of granular matter momentum transferred. Recent studies have shown that the momentum reduction depends upon the frictional interaction between the granular flow and the impacted surface with high coefficient of friction surfaces suffering significantly more momentum transfer than predicted by resolution of the incident momentum onto the inclined plane. This discovery has raised the possibility that inclined surfaces with very low friction coefficients might reduce the impulsive transferred by the impact of ejecta from buried explosions. Here the use of a lubricated sliding plate is investigated as a means for reducing interfacial friction and impulse transfer. The study uses a combination of experimental testing and particle-based simulations to investigate impulse transfer to rigid aluminum surfaces inclined either perpendicular or at 53^{o} degrees to synthetic sand that had been impulsively accelerated to a velocity of 350 -550 m/s. The study shows that impact of this sand with lubricated plates attached to an inclined surface, rapidly accelerates them to a velocity of about 55-70 m/s, and reduces the impulse transferred to the inclined surface. The reduction of impulse by this approach is shown to be comparable to that achieved by changing the inclination of the impact.

Corresponding author: Haydn Wadley

Key words: Granular matter, fluid structure interaction, discrete particle-based simulation

1 Introduction

The design of structures that resist deformation during the impact of soil ejected by a buried explosion is an area of significant research interest [1-8]. The momentum per unit area transferred to a structure by such events can be very large. For example, if a slab of soil of height h with initial density ρ were ejected normal to the surface as a collimated slug with a uniform velocity, v, it has a linear momentum per unit area (specific impulse) $I = \rho v h$. If h = 50 mm, ρ = 2000 kg/m^3, and v = 1000 m/s, the specific impulse would be 100 kPa·s. If such a slug were brought to rest (stagnated with no rebound) against a flat rigid structure oriented perpendicular to the slug propagation direction (at an inclination angle $\alpha = 90^o$), all the momentum would be transferred to the structure causing light structures to suffer significant acceleration. Several experimental [9, 10] and simulation [11] studies have shown that the hydrodynamic pressure applied by the soil to the structure is $\sim\rho_s v^2$, where ρ_s is the density of the soil slab and v its impact velocity. Typically, the soil at the outer surface of the slab is more strongly accelerated, and the slab acquires a distribution of velocities, causing the sand column to stretch (and its density to decrease) as it travels towards a target [9, 12]. If this granular matter were to expand to say three times the initial slab thickness, $\rho_s = \rho/3$ and the average pressure exerted by its impact with the structure would exceed 600 MPa over an impact time of order $3h/v = 150\ \mu s$ for the example above; sufficient to cause substantial deformation and rupture of lightweight structures [3].

Numerous concepts have been proposed for mitigating the effects of soil impact with the underside of vehicles [1-3, 6, 13]. Raising the height of a vehicle above the surface is beneficial since the sand density is reduced by axial and lateral expansion and by additional time for air drag to decelerate the soil particles [12]. The use of a V-shaped hull that reduces the fraction of momentum that is transferred to the impacted surface and increases the time over which the momentum transfer occurs has also been investigated in numerous studies [4, 5, 14-17]. When both approaches are implemented in conjunction with the use of damage resistant materials and structures, the susceptibility of light vehicles to damage by shallow buried landmines can be significantly reduced [18].

To gain a deeper understanding of these granular matter-structure interactions, Uth et al. [19] and Goel et al. [20] recently conducted laboratory studies in which wet sand slugs were launched from a gas gun with velocities of 70-150 m/s and impacted against rigid targets supported on

piezoelectric sensors that enabled measurement of the three reaction force components. This allowed determination of the reaction momentum components for rigidly clamped flat surfaces inclined at either $\alpha = 90^o$ or 45^o to the slug propagation direction, Figure 1(a). The use of stripped sand allowed the axial stretching of the sand slug to be visualized while the rigid targets reaction momentum components in the Z and Y directions (I_T^Z and I_T^Y), resulting from impact of a slug with free field momentum (I_O) travelling in the –Z direction, were determined from the force sensor data. These reaction momenta are exerted by the supports on the rigid structure and are subsequently referred to as the transmitted momentum. The transmitted impulse I_T was determined from that in the two directions using $I_T = \sqrt{(I_T^Z)^2 + (I_T^Y)^2}$. The momentum components were shown to depend upon combinations of the normal, f_n, and tangential, f_t, reaction forces created during impact of the sand with the surface. Since surface friction significantly affected the tangential force, the transferred momentum depended upon both the orientation of the impact surface and the frictional interaction between the particles and this surface.

For a perpendicularly oriented ($\alpha = 90°$) surface, conservation of momentum gives $I_T^Y = 0$ and $I_T = I_T^Z$. The measured transmitted impulse was approximately 1.03 times that of the incident slug (I_O), consistent with a weak rebound (reflection) of sand from the target surface (in the Z direction), Figure 1(b) [20]. Prediction of the momentum transferred to an inclined surface requires knowledge of the tangential force, f_t. However, when the interaction of the sand with the target is frictionless, Goel et al. [20] showed that $I_T^z = I_O \, sin^2 \, \alpha$ and $I_T^y = I_O \, sin \, \alpha \, cos \, \alpha$. For the case of $\alpha = 45^o$, cos α and sin α are identical, so $I_T^Z/I_O = I_T^y/I_O = 0.5$ and therefore $I_T/I_O = 0.707$ which is shown on Figure 1(b) as the resolved (frictionless) limit.

The experimental study confirmed that the momentum transferred to an inclined target was significantly reduced, but exceeded the (frictionless) limit by a substantial amount that depended upon the coefficient of friction between the impact surface and sand. Smooth, very hard surfaces with the lowest friction coefficient were found to acquire the least momentum, while targets with very rough surfaces (or that became very rough during granular impact) acquired substantially more of the sand slugs momentum, Figure 1(b). Furthermore, the changes in momentum transfer arising from variations of the friction coefficient were of a similar magnitude to those achieved by inclining the target. These findings suggest that the use of hard polished coatings applied to the surface of a V-shaped structure might result in substantially reduced momentum transfer. However, the very high contact pressure of soil particles whose impact velocity can exceed 1000

m/s, is likely to cause significant local plastic indentation, erosion and surface roughening during the impact event. Such a dynamic increase of the friction coefficient is therefore likely to limit the benefits of such an approach.

The study described here explores an alternative concept in which granular matter from a planar buried explosive event makes impact with an inclined sacrificial plate that is allowed to slide over a lubricated inclined surface to which it is attached, Figure 2(b). The hypothesis is that when the sliding plate's exterior surface is impacted by soil, it will be accelerated, and acquire a momentum with resolved components perpendicular and parallel to the plate surface. The latter induce plate sliding across a very low friction coefficient interface, reducing the momentum transferred to the underlying structure.

The study uses a recently developed vertical impulse test facility [10, 22] to measure the impulse transferred by an explosively accelerated, 5 cm thick wet sand layer whose distance of travel to the target is systematically varied. The impulse transferred to a flat-bottomed structure oriented normal to the sand impact direction is measured first, and then compared to that for a V-shaped sample whose surfaces are inclined at 53^o to the incident sand direction, Figure 2(a). For uniform sand impact, symmetry of the V-shaped structure dictates that the Y-component of the reaction momentum, I_T^y, will be zero. Momentum conservation further dictates that the Z (vertical) component of momentum, I_T^Z, arising from the impact of granular matter with an incident impulse I_O, can be no less than $I_O\ sin^2\ \alpha$ (the resolved frictionless limit) where α is the angle of inclination. In the absence of significant rebound of the sand, the effective friction force, f_t, at the sample-granular matter interface will dictate how close one can approach the lower limit. Figure 2(b) shows the V-shaped structure equipped with lubricated sliding plates. Impact of sand with these plates transfers momentum, enabling the sliding of the plate along the surface of the underlying target with momentum P_{plate}. In the limiting frictionless interface scenario, the final momentum of the granular matter and sliding plate combination (parallel to the inclined surface) approaches $I_O\ cos\ \alpha$ while the impulse transmitted to the sample (perpendicular to its inclined surface) is $I_T = I_O\ sin\ \alpha$. Since the vertical component of the reaction momentum of the target I_T is $I_T^Z = I_T\ sin\ \alpha$, the vertical impulse component is $I_T^Z = I_O\ sin^2\ \alpha$ (I_O/2 for α = 45^o).

The study experimentally compares the impulse transferred to the three target types as a function of the distance between the sand surface and the target (to vary the average sand velocity, its applied pressure and the duration of the sand impact process). High-speed video imaging is

used to observe the sand-target interaction and motion of the sliding plates after ejection from the targets. Discrete particle-based simulations implemented in the IMPETUS Afea simulation code [21] are used to analyze the experiments and clarify the impulse mitigation mechanism.

2 Experimental methodology

A series of experimental tests were performed at an outdoor explosives test site operated by NEWTEC Services Group, Inc. located in Edgefield, South Carolina. The tests used a vertical impulse test apparatus recently developed and analyzed by Holloman et al. [10, 22]. The tests measured the pressure and impulse transferred to solid aluminum target designs impacted by explosively accelerated wet sand at three standoff distances in an analogous manner to that used to investigate underwater fluid structure interactions [23-25]. The target designs enabled the effect of a sacrificial plate sliding on the momentum transferred to an inclined surface to be compared to that resulting from a change of surface inclination during loading by explosively accelerated wet sand.

2.1 Sample designs and fabrication

Three aluminum targets were developed for the tests, Figure 3. A flat bottom 6061-T6 aluminum target, Figure 3(a), that had an area of 203 mm x 203 mm and thickness of 89 mm, was used to measure impulse transfer for $\alpha = 90^{o}$ sand impacts. The target was milled to shape and then welded to a 305 mm x 305 mm x 6.35 mm attachment plate along the four contact edges with the target, and by a series of 12.7 mm diameter, through thickness, plug welds. Eight holes were also drilled along the outer perimeter of the attachment plate to accommodate 12.7 mm diameter bolts used for attaching the target to the bottom of the vertical impulse test rig.

The second target had the same 203 mm x 203 mm square footprint as the baseline target, but had a V-shaped bottom with two slanted faces inclined at 37° to the horizontal plane, such that the angle between the sand impact direction and the inclined surface was $\alpha = 53°$, Figure 3(b). The geometry of the target was adjusted to ensure that the target mass was identical to the baseline target. As a result, the distance between the apex of the V-bottom and the underside of the attachment was 127 mm compared to 89 mm for the flat-bottomed target.

The third target maintained the same V-shaped bottom as the second with an inclined surface angle, $\alpha = 53°$, and with the same 203 mm x 203 mm square footprint. However, its height was

reduced to accommodate the addition of a pair of 6.35 mm thick, 0.468 kg, sliding 6061-T6 aluminum plates, Figure 3(c). One edge of each of the slider plates was beveled to ensure good apex contact when the pair of slider plates were assembled on the target. Since the slider plates were aluminum, the target with these plates attached was identical in volume and external shape to the V-shaped target, Figure 3(b). The mass of the three target designs was therefore the same.

The sliding plates were held in position using a set of clamps, The *three* Al 6061-T6 targets used for the impulse transfer study: (a) The flat bottom target, (b) the V-shaped target with surfaces inclined at 53^{o} to the incident sand and (c) the V-shaped target with a pair of sliding plates attached.

Figure *4*. Six holes were drilled into each inclined side of the target, and four clamps were bolted onto the target, forming edge rails to ensure the sliding plates remained in place prior to the sand loading. A Molykote M-77 solid lubricant paste from Dow Corning was applied to both interfaces between the sliding plates and the rigid V-shaped target and to the interfaces of the plates with the clamps to minimize friction forces between surfaces when the sliding plate was ejected. This silicone oil based paste has been successfully used between metal/metal contact surfaces and has a base oil viscosity of 125 mm^2/s at 25°C [26]. The impact surface of the baseline and the V-block target (without slider plates) as well as the impact surface of the sliding plates were grit blasted using a coarse grit with a mesh size of 12 to 40. The same grit, spray pressure (690 kPa) and surface modification procedure was used for the impact faces of the three target types so their average surface roughness (5.9 μm) was the same.

2.2 Test apparatus and procedures

The vertical impulse test rig used for the impulsive loading of the targets is shown in Figure 5. This rig consisted of an "A" shaped structural steel frame mounted on a steel base plate that supported a set of four, 5 cm diameter, 2 m long, Kolsky bars, Figure 5(a). The 6061-T6 aluminum Kolsky bars were spaced 10 cm apart in a square pattern and were attached to the rear corners of a test sample, Figure 5. The test rig enables an impulse measurement to be made in one of two ways. One approach allows free sliding of the four bars in a vertical pendulum manner, and the impulse is inferred from the jump height of the pendulum and its mass which can be varied by adding cylindrical plates to the top of the bar system, Figure 5(b). The second approach, utilized here, used a fixed configuration that restrains the pendulum's vertical movement following an impact [10]. In this arrangement, impulse was computed by integrating the axial compressive

stress (pressure) transmitted by the target to the Kolsky bars using strain gauges attached to each bar. To facilitate this arrangement, the top plate of the Kolsky bar assembly shown in Figure 5(b) was securely bolted to the "A-frame" to restrain the pendulum movement when targets attached to the bottom end of the bars were impulsively loaded.

Variations in the standoff distance (defined from the underside of the flat bottom target to the top surface of a test charge) was achieved by altering the height of the explosive test charge located in a sandbox below the target. To standardize the tests, the bottom surface of the attachment plate was held fixed for the three targets at each of the three standoff distances. As a result, the apex of the two V-shaped targets was (127 mm – 89 mm) 38 mm closer to the test charge, Figure 3. An 86 cm x 86 cm x 61 cm A514 grade B steel sandbox contained the sand and explosive charge, Figure 5(b). To reduce ejecta impact with the support structure, a 2.54 cm thick A514 grade steel lid was secured to the top of the steel box during experiments. It contained a 25.4 cm x 25.4 cm square opening through which explosively accelerated sand freely propagated to strike the targets positioned above. The tests were conducted by partially filling the sand box with dry, Type II sand to a depth that would ultimately set the standoff distance for the test. A test charge was then placed on top of this Type II sand and covered with 5.08 cm of water saturated synthetic sand identical to that used by Holloman et al. [10].

The test charge, Figure 6, consisted of a 3 mm thick planar explosive together with a high explosive booster and detonator, all assembled with the aid of a polymer foam plate. The planar energetic material consisted of a 25.4 cm x 25.4 cm, 300 g Detasheet C which consists of 63% pentaerythritol tetranitrate (PETN), 8% nitrocellulose, and 29% acetryl tributyl citrate (ATBC). The Detasheet was positioned on top of a 25.4 cm x 25.4 cm x 3.81 cm thick, low-density polyurethane foam pad. To introduce a more uniform shockwave in the Detasheet, an inverted, truncated, conical hole was drilled in the center of the foam pad and packed with 25 g of C-4 to boost the detonation. Detonation was initiated using a model SP/SM(12-0) instantaneous electric detonator (manufactured by Dyno Nobel Inc., Salt Lake City, Utah) held in position with a 1.9 cm thick sheet of polystyrene foam. The Detasheet charge assembly was placed on the Type II sand whose height was adjusted to result in a standoff distance of 19, 24, or 29 cm, Figure 5(b). A 5.08 cm thick, 25.4 cm x 25.4 cm wide layer of synthetic (Type I) sand, consisting of 150-200 μm diameter soda-lime glass microspheres (grade GL-0201, Mo-Sci Corporation), was placed on the top surface of the Detasheet. This synthetic sand layer had a mass of 4.4 kg and was initially

saturated with an additional 1.2 kg of water. However, in the 10-30 minute time period between setting up and conducting the test, some of the water drained out of the charge assembly. Subsequent measurements indicated that the water content dropped to about 80% of the saturated limit during this time. The total mass of the wet sand at detonation was therefore taken to be 5.36 kg.

A Vision Research Inc., Phantom V7.3 high-speed camera was used to record the nine test events (3 standoff distances for 3 targets). For the sliding plate test, a second camera with a much wider field of view was used to attempt visualization of the sliding plate trajectories as they were ejected into free flight from the rig.

2.3 Kolsky bar instrumentation

Four aluminum Kolsky bars were used to measure the transmitted pressure and deduce the vertical impulse transferred to the targets. A pair of Vishay Micro-Measurements axial-transverse T-rosette strain gages (model CEA-13-125UT-350) were mounted on each Kolsky bar using Vishay AE-10 epoxy adhesive, at a distance of 50.8 cm from the bottom end of the bars, and diametrically opposite to each other [10, 22]. A layer of protective coating (Vishay Gage Kote #5) was applied to protect the gauges and prevent detachment during the experiments. The pair of strain gauges on each bar were connected in a full Wheatstone bridge circuit, and the output voltage on each bar was recorded on separate channels of an analogue to digital converter. The recording of the signal was triggered by the electrical pulse used for initiation of detonation. For protection from the blast and the ejected sliding plates, the instrumentation was placed in a steel box behind a concrete barrier to the side of the vertical rig.

The pressure transmitted to the Kolsky bars was determined from the axial strain of the bars using the method described by Holloman et al. [10]. Briefly, the output voltage, V_o, of the strain gauge forming the full Wheatstone bridge circuit is

$$V_o = \left[\frac{GF * \varepsilon(1+\nu)}{2 + GF * \varepsilon(1-\nu)}\right] V_i$$

where GF = 2.15 is the gage factor, ε is the axial strain in the Kolsky bar, $\nu = 0.33$ is the bar's Poisson's ratio, and $V_i = 10$ V is the input excitation voltage. Hooke's law was used to relate the axial strain to the pressure (axial stress) using the measured Young's modulus for the aluminum

bars, E = 70 GPa. The force transmitted by the rear of the target was found by multiplying the pressure in each bar by its cross sectional area (20 cm^2). The summed forces for the four bars was then divided by the sample's area (0.041 m^2) to determine the pressure transmitted by the test sample. The pressure-time response was digitally recorded for 7 ms and subsequently integrated to determine the impulse-time relationship for each target and standoff distance.

Since the bars were 2 m in length and the strain gauges were positioned 50.8 cm from the impacted end of the bars, elastic wave reflections from the ends of the bars eventually arrived at the sensors and greatly increased the complexity of signal interpretation. Since the speed of the longitudinal wave in Al6061-T6 is 5350 m/s, the first distal reflection arrived at the strain gauges 558 μs after the first direct signal arrival was sensed. A reflection from the impacted end of the bar is expected to arrive at the strain gauges 190 μs later, and would be followed by a second distal reflection 748 μs after the first. Since the bars had a relatively large diameter (to avoid inelastic responses), many Pochhammer-Chree modes [27-29] are expected to contribute to the observed response, and the impulse, determined by integration of the bar pressure, gradually degraded over time.

3 Numerical Discrete Particle Simulations

The experimental results were interpreted with the assistance of particle-based simulations performed using the IMPETUS Afea solver following similar procedures described in detail by Holloman et al. [10] and Kyner et al. [12]. After validation, the simulations were used to determine the impulse that was eventually transmitted to the test structures. They were also used to investigate the activation of sliding plate motion and its affect upon pressure and impulse transfer to the targets.

3.1 Discrete particle methodology

The solver models the transfer of linear momentum through an array of discrete particles whose properties and inter particle contact laws are representative of air, high explosive (HE), and sand [10, 12, 30, 31]. The approach does not address the angular momentum of the particles (it implicitly assumes they have an infinite moment of inertia). Each simulation particle represents many actual particles, and their interactions are governed by spherically symmetric inter particle contact laws. The inter particle contact laws and momentum transfer during the elastic collisions

of air and HE particles are consistent with Maxwell's kinetic theory of gases [30, 31]. Air particles are modeled as an ideal gas and given initial velocities and randomized propagation directions consistent with the Maxwell-Boltzmann distribution. The air particle parameters used by the solver are consistent with an air density of 1.3 kg/m^3, at a pressure of 100 kPa, an initial internal energy of 253 kJ/m^3, and assume a ratio of specific heats $\gamma = 1.4$.

The HE particle parameters for Detasheet C have not been directly determined; however, this explosive material consists of 63% PETN for which particle contact law parameter values are available in the IMPETUS Afea Solver. Since the solver allows the definition of only one HE particle type in a simulation, the PETN and nitrocellulose in the 3 mm thick Detasheet and the C4 booster charge were modelled as PETN. The high explosive model was implemented by filling a 254 mm x 254 mm x 2.4 mm volume with PETN particle properties to represent the PETN and the nitrocellulose, in the 300 g Detasheet. The ATBC plasticizer was not included in this model, resulting in a reduced HE model sheet thickness of 2.4 mm. To simplify the model, the mass of the 25 g C4 booster was represented by a PETN cylinder 0.6 cm in height and diameter. This produced a total mass of PETN HE particles of 0.273 g. The solvers predefined PETN parameters correspond to a density $\rho = 1765$ kg/m^3 and initial internal energy $E_0 = 10.2$ GJ/m^3. The model also specifies the ratio of heat capacities $\gamma = 1.4$, the initial particle solid-fill fraction $b = 0.35$, and the detonation velocity $V_D = 8350$ m/s. During the simulations, detonation was initiated at the center of the bottom surface of the PETN cylinder representing the C4 booster at $t = 0$ μs, whereupon initially stationary detonation particles were released at a time $t = L/V_D$ where L was the particle distance from the detonation location and V_D the detonation velocity.

The normal and tangential soil particle motions following inter particle contact were modeled with a penalty based contact model defined by a linear spring constant k_0, a damping coefficient ξ, and a friction coefficient μ [30, 32]. The contact model used in the solver for both dry and water saturated soil was determined by Borvik et al. [30] using the same 150-200 μm diameter, soda-lime glass microspheres used here. Based on a 60% sand particle fill fraction, the initial density of the dry sand was 1620 kg/m^3. Filling the remaining volume with water leads to fully water saturated sand with a density of 2020 kg/m^3. The water is not explicitly modelled in the solver. Instead, the soil parameters were adjusted by Borvik et al. [30] until the simulation matched the experimental results with water saturated sand. These calibrated parameter values are available as the default parameters for both dry and water saturated soil in the solver, and are listed in Table 1.

The solver also allows user specified parameter values to be utilized. Holloman et al. [10] previously determined soil parameters for a water saturation of 80% corresponding to a wet sand density of ρ = 1940 kg/m^3, and these are also listed in Table 1. The Type I and II sand was modelled using the wet sand parameters in Table 1 with an adjusted contact friction coefficient of 0.08 which was found to give a slightly better match between the simulations and experimental test results.

Table 1. Soil parameters for predefined options in IMPETUS [30] and calibrated wet sand by Holloman et al. [10].

	Density ρ (kg/m^3)	Contact stiffness k_0 (GN/m)	Contact friction coefficient μ	Damping coefficient ξ
Dry	1620	0.4	0.1	0.0
Saturated	2020	4.0	0.0	0.005
Wet	1940	0.76	0.0	0.005

To model the friction created on the impact surface of the grit blasted experimental targets, a soil-structure contact coefficient of friction was defined in the model with a value μ_s = 0.5. The friction coefficient of the lubricated interface between the slider plates and the target surface was modeled using μ_p = 0.05. A convergence study was performed to identify the optimum number of particles, and showed no further improvement in the simulations beyond 2,000,000 particles. The IMPETUS Afea Solver distributed these particles as approximately 70,000 air particles, 10,000 HE particles and 1,920,000 soil particles with exact values differing slightly for each simulation set up (different target and standoff distances). The velocity and density of the soil particles that were explosively accelerated by the detonation event were characterized at 0.5 μs time intervals using four sets of twenty, equidistant virtual spherical sensors ("monitors") each of 5.08 mm radius and located at 2, 7, 12, and 17 cm below the bottom surface of the baseline target.

3.2 Finite element model

The vertical impulse test rig geometry was modeled as a set of finite element (FE) parts, Figure 7(a). The model included the "A-frame" supported vertical pendulum rig and the four, strain gage instrumented Kolsky bars. Figure 7(b) shows a view of the model set up within the sandbox and the attached V-shaped target with aluminum sliding plates. The other two targets are also shown in Figure 7(b). The finite element (FE) geometry was modeled based on the measured dimensions

from the test rig schematic, Figure 5, and the test targets, Figure 3. The four, 5.08 cm diameter Kolsky bars were modeled using the IMPETUS Afea Solver finite element package as multiple cylindrical parts that were merged to form the full, 2 m long Kolsky bars. A 2.54 cm long cylinder region was used at the strain gauge location to determine the axial force between these cylindrical parts and the adjoining parts of the bars. The force on each of the bars was summed and divided by the surface area of the baseline target to determine the pressure transferred to the target. The impulse was calculated as the time integral of the pressure-time waveform. The Kolsky bars were restrained at the top of the rig, and a damping parameter was introduced to better model the oscillatory pressure-time response. The support structure "A frame" and concrete base of the model were defined as rigid structures that remained fixed in space. The sandbox was modeled with dimensions that matched the experimental specifications, including a 25.4 cm x 25.4 cm opening in the lid for the explosively accelerated sand to escape.

After a mesh sensitivity study, the converged FE model of the vertical impulse test rig was meshed with 31,832 elements and 50,221 nodes. Each of the targets was modeled with a finer mesh and was attached to the attachment plate part directly below the Kolsky bars. The baseline flat bottom block was meshed with 3,600 elements and 4,410 nodes. The V-block target was modeled with 480 linear pentahedra elements, 3,560 linear hexahedra elements, and 4,599 nodes. The V-block target with the aluminum slider plates was modeled with 360 linear pentahedra elements, 3,240 linear hexahedra elements and 4294 nodes with slider plates each made up of 520 linear hexahedra elements and 882 nodes.

3.2.1 Material parameters

The material properties for the aluminum AA6061-T6 and A514 steel alloys were defined using the Johnson-Cook constitutive model that defines the von Mises flow stress σ_y as

$$\sigma_y = \left(A + B((\varepsilon_{eff})^n)\right) \cdot \left(1 + C \ln\frac{\dot{\varepsilon}_{eff}}{\dot{\varepsilon}_0}\right) \cdot \left(1 - \left(\frac{T - T_0}{T_m - T_0}\right)^m\right) \quad (1)$$

where the initial yield strength A, hardening parameters B and n, strain rate hardening parameter C and $\dot{\varepsilon}_0$, and thermal softening parameter m are material constants at ambient temperature T_0 and melting temperature T_m. The aluminum parts were modeled using the parameters for AA6061-T6 aluminum obtained by Wadley et al. [3]. The sandbox was modeled as A514 grade B steel using

Johnson-Cook parameters from Johnson et al. [33]. These Johnson-Cook parameters and other material constants for both materials are summarized in Table 2.

Table 2. Johnson-Cook material constants for AA6061-T6 aluminum and A514-grade B steel.

Material	Density and elastic constant			Yield stress and strain hardening			Strain rate hardening		Temperature softening and adiabatic heating		
	ρ ($kg \cdot m^{-3}$)	E (GPa)	ν	A (MPa)	B (MPa)	n	C	$\dot{\varepsilon}_0$ (s^{-1})	T_0 (K)	T_m (K)	m
AA6061	2700	70	0.3	270	98	6	0.001	$5 \cdot 10^{-4}$	293	893	1
A514	7850	210	0.3	796	510	0.26	0.014	$1 \cdot 10^{-2}$	293	1793	1

The foam layers below the Detasheet were included in the simulation using a model built into the solver for an isotropic crushable foam. The foam was modeled with density $\rho = 33$ kg/m^3 and Young's modulus E = 0.9 MPa. A criteria for geometric strain failure was introduced to the foam by defining a failure strain, $\varepsilon_{fail} = 0.1$, at which point the foam lost all strength and was eroded from the simulation.

4 Results and analysis

4.1 Flat bottom target

Figure 8(a) shows a high-speed video image of the initial interaction of explosively accelerated sand (at 0.47 ms after detonation) with the flat bottom target at a standoff distance of 29 cm. The interaction between the high-speed sand front and shock compressed air ahead of the sand caused the development of a sand front instability [12, 34]. This instability results in the formation of sand "fingers" whose tip velocity was up to 18% higher than that of the main sand front. The motion of the sand "fingertips" and the main (continuous) sand front were tracked using the high-speed video images, and the sand position vs time is plotted in Figure 8(b). The main sand front position data was numerically differentiated to obtain the main sand front velocity as a function of time, Figure 8(c). Standard error propagation techniques described in reference [12] were used to estimate the error bars. The data in Figure 8(c) indicate that the main sand front sand was accelerated to a maximum velocity of about 500 m/s during the first 250 μs following detonation before undergoing rapid deceleration (by momentum transfer to air particles) prior to reaching the target at a 29 cm standoff. The estimated main sand front impact times with the flat-bottomed target are shown for each of the standoff distances in Figure 8(c), and each incident main sand front speed is listed in Table 3.

A simulation of the test is shown in Figure 9 and allows the important physical processes involved in (initially) planar sand front propagation towards the target to be investigated. The figure shows the sand particles' positions and color codes their vertical (Z-direction) velocity at selected times after detonation. The sandbox lid and the test fixture hardware have been hidden in these images. Detonation of the HE layer resulted in the launching of a compressive shock front into the 5 cm thick layer of wet sand. This front can be easily seen in the sand particle velocity data at 30 μs after detonation, Figure 9(a). The wet sand shock speed was estimated to be 1690 m/s which is consistent with previous estimates by Holloman et al. [10] for the same sand. Upon reaching the air–sand interface, the compressive shock was reflected back into the sand as a release wave. To conserve momentum, this resulted in outward spallation of the sand particles from an interface that propagated inwards through the sand layer, Figure 9(b). The first particles released in this manner had a velocity in excess of 500 m/s while those launched later were significantly slower, Figure 9(c). As a result, the initially 5 cm thick slab of sand was stretched in length as it advanced perpendicular to the original plane of the sand surface, and therefore in a manner consistent with recent sand slug experiments [9, 35]. Some lateral expansion of the sand also occurred. Later in the process, Figure 9(d-f), expanding high pressure detonated HE particles (not shown) "pushed" the slower (lower) end of the sand slab towards the target.

The simulated sand particle position image at 0.45 ms after detonation, Figure 9(f), corresponds to the high-speed video image shown in Figure 8(a). The impact of the fastest sand particles (red) with the bottom of the target is consistent with the experimental observation of sand fingertip impacts in Figure 8(a). However, the topology of the fingers that are initiated by an interfacial instability [34] were not resolved in the simulation. Alternative analysis methods capable of analyzing the aerodynamic forces upon these highly deformable granular structures (travelling at a velocity approaching the Mach 2 range into shock compressed air) are necessary for this.

The position of the main sand front at various time steps was measured using the four rows of sensors shown in Figure 9(a). The main sand front position data is shown as a function of time in Figure 8(b), and the corresponding velocity versus time response is shown in Figure 8(c). These simulation results can be seen to be in good agreement with the experimental observations. The main sand front was strongly accelerated by the detonation, but then began to decelerate due to

momentum transferring collisions with background air particles. This resulted in the attainment of a maximum main sand front velocity of ~500 m/s at about 0.2-0.3 ms after detonation as the sand front passed through the 19 cm standoff distance location. As the standoff distance was increased, the sand that reached the target surface had suffered more air drag, resulting in a main sand front velocity of about 350 m/s by the time it reached the sample at the 29 cm standoff distance, Figure 8(c). This, combined with greater stretching (and more lateral expansion) at later times, resulted in a reduction of sand density as the standoff distance increased.

The sand particles that impacted the flat surface suffered a weak reflection and began to rebound in the –Z direction. However, they then suffered impact with later arriving particles which resulted in accumulation of particles against the target surface, consistent with calculations of sand slug impacts on normally oriented rigid targets [11, 36]. Further particle impacts eventually caused particles to flow radially outwards, towards and past the edges of the target surface, Figure 9(i). Because of the lateral stretching of the sand, a small fraction (5-10%) of the sand particles did not impact the target but instead impacted the underside of the attachment plate, Figure 9(h) and (i). This is likely to increase the impulse transferred to the instrumented Kolsky bars above that applied by sand impact with the target, and is corrected for in Section 5.

The pressure-time signals experimentally determined from the Kolsky bar strain gauge data are plotted for each standoff distance for the flat target and compared with simulations in Figure 10. Since signal reflections from the ends of the bars complicate the data and the damping of the Kolsky bars was not well understood, data is only plotted for the first 2.15 ms of loading corresponding to a time shortly after the 2nd distal reflection at the Kolsky bar sensors for the 29 cm standoff distance test. The first distal reflection arrived 558 μs after the initial (direct) signal arrival while the second reflection was delayed by an additional 748 μs. These times are indicated for each standoff distance on Figure 10.

At each standoff distance, the pressure exhibits a sharp rise to an initial peak pressure (reported in Table 3) followed by a secondary peak of equal or greater value. The simulated responses are in generally good agreement with the measurements. Increasing the standoff distance delayed the rise in pressure due to the delay in impact time that resulted from the increased distance and declining velocity of sand that impacted the sample. The initial peak pressure was also influenced by standoff distance falling from 13.0 MPa at 19 cm to 7.1 MPa at the 29 cm standoff distance.

Table 3. Incident main sand front speed at the time of impact with the flat bottom target and experimentally measured initial pressure peaks and impulse rates for the three targets for each standoff distance.

Standoff distance (cm)	Sand speed (m/s)	Flat block		V-block		V-block with Al slider plates	
		Initial peak pressure (MPa)	$\frac{dI}{dt} = \dot{I}$ (MPa)	Initial peak pressure (MPa)	$\frac{dI}{dt} = \dot{I}$ (MPa)	Initial peak pressure (MPa)	$\frac{dI}{dt} = \dot{I}$ (MPa)
19	510	13.0	11.6	8.4	8.0	8.1	7.8
24	440	8.7	7.6	5.8	5.0	3.4	3.3
29	310	7.1	6.4	4.7	4.2	4.1	3.9

The transmitted impulse-time plots (obtained by integrating the pressure-time plots) are shown in Figure 10(b), (d) and (f) for the three standoff distances. The impulse plots show an initial rise in slope with a slope change between the first and second reflection arrival times. The impulse rate, $\dot{I}$, was determined from the initial slope of the impulse-time response prior to the arrival of the first distal reflection and is summarized in Table 3. The impulse rates while slightly lower than the initial peak pressures, consistently declined with standoff distance. The arrival times of the first and second distal reflection at the strain gauge location are shown for each impulse plot. The measured impulse at each of these times, indicated by dotted lines in Figure 10, is summarized for each standoff distance in Table 4. The simulated data is also shown on Figure 10 and agrees very well with the experiments. The impulse accumulated up to the arrival of the first distal reflection decreased rapidly with standoff distance due to a combination of the drop in sand particle velocity, Figure 8(c), and axial and lateral stretching of the sand column [10]. These impulse values are shown as a function of standoff distance in Figure 11.

Table 4. Experimentally measured transmitted impulses at the arrival time of the first and second distal reflections for the three targets.

Standoff distance (cm)	Flat block		V-block		V-block with Al slider plates	
	Transferred impulse		Transferred impulse		Transferred impulse	
	1^{st} distal reflection (kPa·s)	2^{nd} distal reflection (kPa·s)	1^{st} distal reflection (kPa·s)	2^{nd} distal reflection (kPa·s)	1^{st} distal reflection (kPa·s)	2^{nd} distal reflection (kPa·s)
19	7.1	11.9	4.2	11.2	3.4	9.5
24	4.1	11.2	2.2	9.2	1.8	8.2
29	3.5	10.7	1.8	7.3	1.5	5.3

4.2 V-shaped target

High-speed video images of sand impact with a V-block target at a standoff distance of 29 cm are shown in Figure 12. Careful examination of the images in Figure 12(d)-(e) shows reflection of the sand off the edge of the target (indicated by white lines) parallel to the inclined surface of the V-block. However, important details are obscured by the sand that travelled between the target and camera. Results from a simulation of the test are shown in Figure 13 and can be used to better understand the test results. The fastest sand began to first impact the target at about 0.45 ms after detonation. The simulation in Figure 13(a) shows sand particle locations at about the same time as the experimental image in Figure 12(a). It shows that the fastest sand had contacted the target in a manner consistent with the experimental image. The subsequent simulations show that sand particles were forward reflected from the target's inclined faces and travelled towards the outer edges of the target. Many of these reflected particles suffered collisions with later arriving incoming particles causing their redirected trajectory to remain close (and parallel) to the inclined target surface. Some of these particles can be seen leaving the target in Figure 13(d). As time progressed, the concentration of the near surface reflected particles increased, and a thin line of particles flowing away from the target edge can be clearly seen in Figure 13(e) and (f) consistent with experimental observations, Figure 12(d) and (e). The accumulation of particles is clearly seen in Figure 13(g) and (h) with the densest region of the propagating sand impacting the target at between 2.0 and 2.8 ms after detonation. It remained close to the inclined edge as it flowed parallel to the surface and then beyond the V target edge. Once again, a small fraction of the sand particles made impact with the underside of the attachment plate rather than the test target. Their impulse would have been added to that of the samples in both the experimental and simulated transmitted impulse data measured by the Kolsky bars.

Figure 14 shows the measured and simulated pressure-time waveforms and the integrated impulse-time plots for the V-shaped target. The simulated and measured signal arrival times and waveforms are in good agreement. Like the experimental results, the simulated signal shows an initial pressure peak followed by a second pressure peak of equal or greater value. When these results are compared to those for the flat bottom sample, Figure 10, it is evident that the rise time of the V-block target pressure was substantially longer. This arose because of the variation in sand propagation distance (and therefore impact time) with lateral position for the V-block target. The V-block target pressure waveforms again exhibited two peaks with the peak positions

corresponding to the arrival of sequential Kolsky bar distal reflections. The maximum pressure attained during the first peak is summarized in Table 3. It decreased from 8.4 MPa at a standoff distance of 19 cm to 4.7 MPa at the 29 cm standoff distance consistent with a reduction in particle velocity and decrease in density (due to longitudinal and lateral spreading of the sand particles) with increasing standoff distance. Since the apex of the V-block target was 3.8 cm closer to the sand surface than the flat bottom geometry sample, Figure 3, the apex of the V-shaped targets at a nominal standoff distance of 19 cm was only ~15 cm from the Datasheet surface. At this standoff, examination of Figure 9(c) and (d) shows that the sand first arrived at the apex location at approximately 0.2 ms after detonation and with a velocity near the peak in Figure 8(c). The initial signal arrival time at the strain gauge location is slightly earlier for the V-block targets compared to the arrival times of the flat bottom target, consistent with this observation. The measured impulse transmitted by the V-block target at the first and second distal reflection arrival times is summarized in Table 4, and is plotted against standoff distance in Figure 11. Like the flat bottomed sample, the impulses fell sharply with standoff distance.

4.3 V-shaped target with sliding plates

Figure 15 shows high-speed video images of the impact of the sand with the V-block target with attached aluminum slider plates (using the same time sequence as Figure 12) for a standoff distance of 29 cm. The sand fingers had already begun to make contact with the target in the image collected at 0.58 ms after detonation, Figure 15(a). While redirection of the sand upon impact is evident in Figure 15(d)-(f), details are again obscured by intervening sand. A simulation of the test is shown in Figure 16. Initial impact of sand fingers with the sample apex (not shown) occurred at approximately 0.45 ms. The result shown in Figure 16(a) at 0.57 ms after detonation is consistent with the experimental observation, Figure 15(a), of fastest sand contact with the sample at this time. During the following 0.27 ms of loading, Figure 16(a)-(d), the slider plates acquired sufficient impulse to begin sliding at approximately 0.84 ms after detonation, Figure 16(d). Figure 16(d)-(f) show that the sand impact with the slidable plates caused continued acceleration of the sliders resulting in exposure of the V-block apex to impact by late arriving sand. Some sand particles again missed the V-block and made impact with the underside of the attachment plate. However, as the sliding plates began to propagate outwards, they intersected this sand and began to shield the underside of two areas of the attachment plate from further impact (and impulse), Figure 16(g)-(i). Departure of the plates from the rigid V-block surfaces is seen in

Figure 16(i) to have occurred at 3.6 ms after detonation. The ballistic trajectory of one of the sliding plates for this 29 cm standoff distance test was successfully tracked using the wider field of view camera. Images from this camera have been overlaid at approximately 100 ms time intervals in Figure 17 to show the sliding plate's parabolic trajectory (and plate rotation). The sliding plate was subsequently recovered 12.5 m to the right of the vertical rig apparatus at a location orthogonally offset by 1.8 m towards the camera.

High-speed video observations of the interaction of sand at a 19 cm standoff distance are shown in Figure 18. Figure 18(a) is the initial set-up at the instant of detonation. It shows the support rig, the steel sandbox, the Kolsky bar system (including its strain gauges), the trigger wire for detonation initiation, the V-target with aluminum sliding plates, and the concrete barrier protecting the instrumentation. Figure 18(b) shows the sand position at 0.3 ms after detonation. The inset shows that contact of sand with the apex of the target had already occurred, consistent with the prediction of Figure 9 that the first sand would arrive at approximately 0.2 ms after detonation. Subsequent interactions between the sand and target shortly thereafter are hidden by reflected sand and (black) detonation products. Nevertheless, Figure 18(c) collected at 1.2 ms after detonation shows that substantial sand reflection from the V-shape of the target had occurred. The sand then completely obstructed the view of the target until about 35 ms after detonation. In Figure 18(e) and (f), the sand had expanded to a sufficiently low density that the sliding plates could be seen after their ejection from the target. Their initial position is identified, and dotted lines are provided to indicate their probable trajectory to their first observed positions. The sliding plates were eventually recovered from a location 39 m from the original position.

The simulation of the 19 cm standoff distance test can be used to infer the targets response sequence. Figure 19 shows particle progression, impact with the target, and slider plate ejection for the 19 cm standoff distance test. In Figure 19(b), the detonation has transmitted a compressive shock through the wet sand. This is subsequently reflected at the air-sand interface resulting in spallation of fast sand from the interface. Figure 19(c) shows that the accelerated sand had begun to impact the target slightly before 0.3 ms after detonation, consistent with experimental observations, Figure 18(b). Plate sliding began shortly before Figure 19(e) at approximately 0.6 ms after detonation. At this standoff distance, the sliding plates escaped the target between Figure 19(g) and (h) at approximately 2.3 ms after detonation. Once the slider plate is impacted and

accelerates outward, the V-target apex and underlying inclined surfaces become exposed to late arriving sand impacts.

The simulations indicated that the time taken for the slider plates to slide halfway off the target surface increased with standoff distance from approximately 1.5 to 2.5 ms. The plate escape times at each of the standoff distances were determined from the simulations and are summarized in Table 5, together with their horizontal (V_Y) and vertical (V_Z) velocity components, their departure speed, and their Z-component momentum and impulse at the time of escape. As the standoff distance increased, the sliding plate velocity and momentum decreased consistent with the reduction in sand velocity (Figure 8(c)) and density resulting from collisions of sand particles with air and the axial and lateral stretching of the sand plume. It is interesting to observe the accumulation of the sand particles near the sliding plates in Figure 19(e) to (i), indicating cessation of motion in the reference frame of the sliding plates and the end of momentum transfer to the plates. This phenomenon was also observed for 29 cm standoff distance in Figure 16(g) and (h).

Table 5. Simulation predicted slider plate escape time for a V shaped target, together with the plates Y and Z component velocities and plate speed at the time of escape. The P_Z momentum and I_Z impulse component of the each plate is also given.

Standoff (cm)	Escape time (ms)	V_Y (m/s)	V_Z (m/s)	Plate speed V (m/s)	Z-plate momentum P_Z (N·s)	Z-plate impulse I_Z (kPa·s)
19	2.60	53	43	69	20	0.97
24	2.97	51	41	66	19	0.93
29	3.45	43	35	57	16	0.79

The measured and simulated pressure-time waveforms for the V-block targets with the aluminum slider plates are shown for each standoff distance in Figure 20. The pressure waveforms had a similar initial slope and peak pressure to the V-block target, Table 3. The transmitted impulse at the first and second distal arrival times are also listed in Table 4, and their dependence upon standoff distance shown on Figure 11. While the maximum pressures of the first peaks were similar to those of the tests conducted on V-block samples without a sliding plate, the impulses later in the loading process were substantially reduced as the inertia of the sliding plates was overcome.

5 Discussion

The experimental study has confirmed that significant reductions in the pressure applied by impact of granular matter with a target can be achieved by reducing the inclination of impact and increasing the standoff distance, Table 3. Integration of the measured pressure up to the arrival of the first distal reflection, Table 4 and Figure 11(a), also showed that the impulse transmitted to the targets decreased with reduction of incidence angle and increase in standoff distance. For example, at a standoff distance of 19 cm, the impulse fell from 7.1 kPa·s for the flat bottom target to 4.2 kPa·s for the V-block target. The combination of increasing the standoff distance from 19 to 29 cm and reducing α from 90^o to 53^o decreased the impulse from 7.1 kPa·s to only 1.8 kPa·s. The discrete simulations gave similar peak pressures and impulses to those measured, Figure 10 and Figure 14, supporting their use for interpretation of the tests.

The spatial distribution of the impulse transferred to the samples is shown in Figure 21 for each standoff distance. Note that some impulse was also transmitted to the underside of the attachment plates supporting each target (its contribution to the transmitted impulse will be estimated below). The impulse applied to the flat-bottomed target was uniformly distributed across the surface of the impact face of the target, and declined as the standoff distance was increased. The impulse transmitted to the V-block target was much more concentrated near the apex of the target. Recall from Figure 7(b) that the distance between the apex of the V-block target and the explosive sheet was 3.8 cm less than that to the surface of the flat-bottomed sample. Even though this local standoff distance was smaller, the impulse applied to the inclined surfaces of the V-block was less than to the flat-bottomed target because the reflected sand retained a significant fraction of its incident momentum in the Z direction.

The mechanisms responsible for the reductions of pressure and impulse with standoff distance for $\alpha = 90^o$ targets have been analyzed by Holloman et al. [10] and shown to result from axial and lateral spreading of the granular medium, and reductions in its velocity due to momentum transferring collisions with air particles. This interpretation is consistent with the simulations shown in Figure 9. The surface inclination effect observed here in both the experimental and simulation results also support the observations of Goel et al. [20], Figure 1(b). By avoiding the arrest or rebound reflection of a granular flow against the target, a reduction of α from 90^o to 53^o reduced the impulse by a factor of 0.4-0.5 at the first distal reflection, Figure 11(a).

The experimental and simulation results, Figure 11, indicated that a further reduction in the applied pressure and the I_T^Z component of transferred momentum was achieved by allowing the lubricated sliding of a pair of 6.35 mm thick plates attached to the V-shaped target. Since the measured and simulated pressures and impulses are in very good agreement, the simulations can be used to analyze the mechanisms of interaction of the targets with the granular medium. The effect of the sliding plates upon the impulse distribution on the V-shaped structure is also shown in Figure 21. The majority of the impulse was transmitted to the apex end of the sliding plates with the underlying V-block directly receiving only a small fraction of the incident impulse at all standoff distances. The time dependent impulse transmitted to the V-block and sliding plate V-targets has been calculated for the first 4 ms of loading and is shown in Figure 22(a) for the three standoff distances. The difference in transmitted impulse between the two target types was initially small, but then began to grow after a delay time that increased with standoff distance. This delay in impulse reduction is consistent with the time taken for the initiation of plate sliding.

The distance the sliding plate moved is scaled by the length of the inclined edge of the V-block target, E_i = 12.7 cm, and the normalized displacement is plotted versus time in Figure 22(b). It shows that the distance the plates had moved, ξ, decreased with increasing standoff distance (i.e. with decrease in incident impulse). The escape distance is shown by a dotted grey line along with the points of intersection with the slider plate distance at each standoff, and vertical dotted lines indicate the slider plate escape times which were summarized in Table 5. This analysis rationalizes the experimental results shown in Figure 11 where the impulse accumulated up to the time of arrival of the first distal reflection (558 μs after the direct signal reached the strain gauges), showed little effect of the sliding plates, but their beneficial effect then increased over time as seen in Figure 11(b) (748 μs later).

The I_T^Z component of impulse transferred to each target design after 4 ms of loading can be calculated from the simulated strain gauge pressure and is plotted as a function of standoff distance in Figure 23(a). This (total) impulse is the sum of the impulse applied to the test targets and that applied to the underside of the attachment plate, Figure 21. This attachment plate impulse varied from 1 to 3 kPa·s, and resulted from the lateral expansion of the sand front beyond the width of the test targets, Figure 9, Figure *13*, and Figure *16*. It is plotted on Figure 23(b) for the three targets at each standoff distance. The impulse transferred to only the target surfaces is summarized in Table 6 and is also plotted on Figure 23(b). It shows that the reduction of impulse by the use of

the sliding plates was approximately a half the reduction achieved by the change of incidence angle.

To quantify the effects of the target geometry and use of a sliding plate for buried charge test geometry studied here, the ratio of the transmitted to incident impulse for each target design is also shown in the Table 6. It can be seen that the ratio of the transmitted to incident impulse for the flat bottomed target was approximately 1.02 while that to the V-block was 0.85 and the target with sliding plates was 0.76. The Z-component impulse of each slider plate at its time of escape from the targets was calculated by dividing the product of the plate mass and V_Z velocity component (Table 5) by the area normal to the plate (203.2 mm x 101.6 mm). The results indicate that approximately 8% of the incident impulse was transferred to each slider plate as it escaped the V-block base target. The inclined V-block target (α=53°) reduced the impulse transferred to the normally oriented target (α=90°) by about 17%. An additional impulse reduction of approximately 11% was achieved by the use of sliding plates.

Table 6. Simulated impulse and normalized impulse applied to the three target designs for each standoff distance.

Standoff	I_O	Flat bottom		V-block ($\mu_s = 0.5$)		V-block with slider plates	
		I_T^Z	I_T^Z/I_O	I_T^Z	I_T^Z/I_O	I_T^Z	I_T^Z/I_O
(cm)	(kPa·s)	(kPa·s)		(kPa·s)		(kPa·s)	
19	11.10	11.40	1.03	9.48	0.85	8.71	0.78
24	10.93	11.00	1.01	9.06	0.83	8.21	0.75
29	10.44	10.71	1.03	8.97	0.86	7.83	0.75

To compare the results in Table 6 with those of Goel et al. [20], the impulse ratios I_T^Z/I_O are plotted versus standoff distance in Figure 24 (the incident main sand front speed for each standoff is summarized in Table 3). The reduction of impulse resulting from a decrease of the inclination angle from 90^o to 53^o can be clearly seen. However, the simulations indicate that this "inclination effect" is dependent upon the friction coefficient the sand particles and target surface. Inclined target impacts with a friction coefficient of μ_s = 0.5 result in an impulse ratio reduction from 1.02 to 0.85 whereas frictionless impact (with a friction coefficient μ_s =0.0) results in an impulse reduction from 1.02 to 0.72. This change of impulse is shown as the particle friction effect in

Figure 24, and confirms the significant effect of surface friction reported by Goel et al. [20], Figure 1(b).

Examination of Figure 24 shows that the impulse ratios for tests with the sliding plates (solid triangles) resulted in a transferred impulse ratio of 0.76 which was higher than the predicted value of 0.72 for the frictionless V-block target (the red filled circles). Examination of Figure 21 shows that some of the impulse transferred to the sliding plate targets impacted the apex after region beneath the plate (after it had slid past these regions). These test samples therefore experienced two phases of loading. During Phase I, the sand impacted the sliding plates attached to the V-block target, transferring some of their incident momentum to the plates and thereby initiating low friction sliding motion across the surface of the underlying V-block target. The exposed surface of underlying V-block base was then impacted by later arriving (lower velocity) Phase II particles. The Phase II impulse transferred to the underlying V-block target varied from 1.8 kPa·s at a 19 cm standoff distance to 2.13 kPa·s at a standoff distance of 29 cm. When the impulse associated with this Phase II sand impact was excluded from the analysis, the sliding plate impulse ratio dropped to the simulated frictionless particle V-block result (~0.72).

However, the reduction of impulse ratio to 0.72 in the frictionless limit for impacts with the sliding plate V-block target substantially exceeded the resolved momentum for an inclination α = 53° for which momentum conservation gives $I_T^Z/I_O = 0.64$. This discrepancy arises because some of the impulse in the buried tests analyzed here was transferred to the test samples by gaseous (air or high explosive) particles, which have a very weak frictional interaction with the targets. Table 7 shows the contributions to the impulse transferred to the V-block target for the three particle types (sand, air, and HE). The impulse applied by the air and HE particles was approximately 8.5% of the total impulse. This is roughly the difference between the frictionless impulse ratio (open circles) and the resolved frictionless limit. When the impulse contribution of gaseous particles is removed from the simulations, the (red square) results are very close to the resolved frictionless limit of 0.64.

Table 7. Impulse transferred to the V-block target by each particle type (sand, air, HE). The sand particles were modelled with a friction coefficient $\mu_s = 0.0$.

	V-block ($\mu_s = 0.0$)			
Standoff Distance (cm)	Total (kPa·s)	Sand (kPa·s)	Air (kPa·s)	HE (kPa·s)

19	8.16	7.56	0.55	0.04
24	7.77	7.10	0.60	0.07
29	7.56	7.00	0.65	0.10

6 Concluding Remarks

A combined experimental and discrete particle based simulation approach has been used to investigate impulse transfer from granular matter with an incident velocity of 350-550 m/s to rigidly supported targets. The study investigated both the effect of target inclination angle using designs with $\alpha = 90°$ (normally oriented) to $\alpha = 53°$ and a sliding plate concept that reduced the effects of friction during loading by impulsively accelerated sand particles. The inclination angle investigation confirmed the reduction in impulse transferred to an inclined surface was dependent upon frictional interactions between the particles and the target surface. A novel target design that implemented lubricated (low friction) sliding plates on the inclined target surface was successfully tested. Simulations revealed that these plates acquired a velocity between 55-70 m/s from momentum transfer by the incident granular impact. This novel lubricated sliding plate design led to further reductions in impulse that can be comparable to that achieved by changing the inclination angle.

Acknowledgements

The authors are very thankful for the technical support and insight of Keith Williams (NEWTEC Services Group Inc.). Further, we would like to acknowledge Dr. Kumar Dharmasena for sample fabrication designs and both Dr. Dharmasena and Tommy Eanes for experimental assistance and guidance. This research was funded by the Defense Advanced Research Projects Agency (DARPA) under grant number W91CRB-11-1-0005 (Program manager, Dr. J. Goldwasser).

References

[1] K.P. Dharmasena, H.N. Wadley, T. Liu, V.S. Deshpande, The dynamic response of edge clamped plates loaded by spherically expanding sand shells, International journal of impact engineering, 62 (2013) 182-195.
[2] J. Rimoli, B. Talamini, J. Wetzel, K. Dharmasena, R. Radovitzky, H. Wadley, Wet-sand impulse loading of metallic plates and corrugated core sandwich panels, International journal of impact engineering, 38 (2011) 837-848.
[3] H.N. Wadley, T. Børvik, L. Olovsson, J.J. Wetzel, K.P. Dharmasena, O.S. Hopperstad, V. Deshpande, J.W. Hutchinson, Deformation and fracture of impulsively loaded sandwich panels, Journal of the Mechanics and Physics of Solids, 61 (2013) 674-699.
[4] D. Fox, X. Huang, D. Jung, W. Fourney, U. Leiste, J. Lee, The response of small scale rigid targets to shallow buried explosive detonations, International journal of impact engineering, 38 (2011) 882-891.
[5] R.R. Sahu, P.K. Gupta, Blast diffusion by different shapes of vehicle hull, International Journal of Automotive Engineering and Technologies, 2 (2013) 130-139.
[6] E.G. Pickering, S.C.K. Yuen, G. Nurick, P. Haw, The response of quadrangular plates to buried charges, International journal of impact engineering, 49 (2012) 103-114.
[7] D.M. Bergeron, R. Walker, C. Coffey, Detonation of 100-gram Anti-personnel Mine Surrogate Charges in Sand, a Test Case for Computer Code Validation, National Defence, Defence Research Establishment Suffield, 1998.
[8] W. Fourney, U. Leiste, R. Bonenberger, D. Goodings, Explosive impulse on plates, Fragblast, 9 (2005) 1-17.
[9] S. Park, T. Uth, N. Fleck, H. Wadley, V. Deshpande, Sand column impact onto a Kolsky pressure bar, International journal of impact engineering, 62 (2013) 229-242.
[10] R.L. Holloman, V. Deshpande, H.N.G. Wadley, Impulse transfer during sand impact with a solid block, International journal of impact engineering, 76 (2015) 98-117.
[11] S. Pingle, N. Fleck, H. Wadley, V. Deshpande, Discrete element calculations of the impact of a sand column against rigid structures, International journal of impact engineering, 45 (2012) 74-89.
[12] A. Kyner, K. Dharmasena, K. Williams, V.S. Deshpande, H.N.G. Wadley, High intensity impulsive loading by explosively accelerated granular matter, International Journal of Impact Engineering, (2017 (Submitted)).
[13] N. Jacob, G. Nurick, G. Langdon, The effect of stand-off distance on the failure of fully clamped circular mild steel plates subjected to blast loads, Engineering Structures, 29 (2007) 2723-2736.
[14] S. Chung Kim Yuen, G.S. Langdon, G.N. Nurick, E.G. Pickering, V.H. Balden, Response of V-shape plates to localised blast load: Experiments and numerical simulation, International journal of impact engineering, 46 (2012) 97-109.
[15] C.E. Anderson, T. Behner, C.E. Weiss, Mine blast loading experiments, International journal of impact engineering, 38 (2011) 697-706.
[16] W. Fourney, H. Leiste, A. Hauck, D. Jung, Distribution of specific impulse on vehicles subjected to IED's, International Journal for Blasting & Fragmentation, 4 (2010) 117-134.
[17] M.-A. Saeimi-Sadigh, A. Paykani, A. Afkar, D. Aminollah, Design and energy absorption enhancement of vehicle hull under high dynamic loads, Journal of Central South University, 21 (2014) 1307-1312.
[18] C. Lester, Protection of Light Skinned Vehicles Against Landmines-A Review, in, DTIC Document, 1997.
[19] T. Uth, H.N.G. Wadley, V.S. Deshpande, The effect of inclination and stand-off on the dynamic response of beams impacted by slugs of a granular material, International Journal of Solids and Structures, 56–57 (2015) 154-174.
[20] A. Goel, T. Uth, H.N.G. Wadley, V.S. Deshpande, Effect of surface properties on momentum transfer to targets impacted by high velocity sand slugs, Submitted for publiction., (2016).

[21] A.G. Hanssen, L. Olovsson, Welcome to IMPETUS AFEA, in, IMPETUS AFEA, Flekkefjord, Norway.
[22] R.L. Holloman, V. Deshpande, H.N.G. Wadley, Impulse transfer during sand impact with a cellular structure, International journal of impact engineering, 82 (2015) 36-58.
[23] Z. Wei, K. Dharmasena, H. Wadley, A. Evans, Analysis and interpretation of a test for characterizing the response of sandwich panels to water blast, International journal of impact engineering, 34 (2007) 1602-1618.
[24] K. Dharmasena, D. Queheillalt, H. Wadley, P. Dudt, Y. Chen, D. Knight, A. Evans, V. Deshpande, Dynamic compression of metallic sandwich structures during planar impulsive loading in water, European Journal of Mechanics-A/Solids, 29 (2010) 56-67.
[25] K. Dharmasena, D. Queheillalt, H. Wadley, Y. Chen, P. Dudt, D. Knight, Z. Wei, A. Evans, Dynamic response of a multilayer prismatic structure to impulsive loads incident from water, International journal of impact engineering, 36 (2009) 632-643.
[26] Molykote M-77 Solid Lubricant Paste, in: Form No. 71-0186E-01, Dow Corning, 2014.
[27] A.D. Puckett, M. Peterson, Individual longitudinal Pochhammer-Chree modes in observed experimental signals, Acoustics Research Letters Online, 6 (2005) 268-273.
[28] J.A. Simmons, E. Drescher-Krasicka, H. Wadley, Leaky axisymmetric modes in infinite clad rods. I, The Journal of the Acoustical Society of America, 92 (1992) 1061-1090.
[29] R. Davies, A critical study of the Hopkinson pressure bar, Philosophical Transactions of the Royal Society of London A: Mathematical, Physical and Engineering Sciences, 240 (1948) 375-457.
[30] T. Børvik, L. Olovsson, A. Hanssen, K. Dharmasena, H. Hansson, H. Wadley, A discrete particle approach to simulate the combined effect of blast and sand impact loading of steel plates, Journal of the Mechanics and Physics of Solids, 59 (2011) 940-958.
[31] L. Olovsson, A.G. Hanssen, T. Børvik, M. Langseth, A particle-based approach to close-range blast loading, European Journal of Mechanics - A/Solids, 29 (2010) 1-6.
[32] V. Deshpande, R. McMeeking, H. Wadley, A. Evans, Constitutive model for predicting dynamic interactions between soil ejecta and structural panels, Journal of the Mechanics and Physics of Solids, 57 (2009) 1139-1164.
[33] G.R. Johnson, W.H. Cook, A constitutive model and data for metals subjected to large strains, high strain rates and high temperatures, in: Proceedings of the 7th International Symposium on Ballistics, The Hague, The Netherlands, 1983, pp. 541-547.
[34] K. Kandan, S. Khaderi, H.N.G. Wadley, V.S. Deshpande, Instabilities in shock loaded granular media, In progress, (2016).
[35] T. Uth, V. Deshpande, Response of clamped sandwich beams subjected to high-velocity impact by sand slugs, International journal of impact engineering, 69 (2014) 165-181.
[36] T. Liu, N. Fleck, H. Wadley, V. Deshpande, The impact of sand slugs against beams and plates: Coupled discrete particle/finite element simulations, Journal of the Mechanics and Physics of Solids, 61 (2013) 1798-1821.

Figure 1. (a) A schematic illustration of the impact of a sand column of length h and momentum mv_o with an inclined coated surface. (b) The measured effect of target surface inclination and roughness upon the fraction of the incident momentum transferred to the target. The fraction of the incident momentum resolved onto the frictionless $\alpha = 45°$ plane is also shown as the resolved limit.

Figure 2. Reaction momenta following impact of a granular matter slab of thickness h with (a) a V-block target and (b) a V-shaped target with the slider plates attached.

Figure 3. The three Al 6061-T6 targets used for the impulse transfer study: (a) The flat bottom target, (b) the V-shaped target with surfaces inclined at 53^o to the incident sand and (c) the V-shaped target with a pair of sliding plates attached.

Figure 4. The sliding plate target geometry showing the use of four edge clamps to guide the sliding plates during sand impact.

Figure 5. (a) Schematic illustration of the vertical impulse test rig with a flat-bottomed solid aluminum target attached. (b) An expanded view of the interior of the steel box, the test charge design, the sample location, the standoff distance, and the strain gauge location on the Kolsky bars.

Figure 6. Schematic illustration of the test charge.

Figure 7. (a) A schematic illustration of the FE model of the vertical impulse test rig. Each color-coded part used a different model and material combination. (b) The simulation geometry for the inside of the sandbox and the attached V-block target with sliding plates at a standoff distance of 29 cm. The geometries of the flat block and V-block targets are also shown.

Figure 8. (a) A photograph of the sand front at 0.47 ms after detonation showing the main front position and the presence of sand fingers for a test with the flat bottom sample at a standoff distance of 29 cm. (b) The measured and simulated main sand front position versus time and measured fingers position versus time. (c) The measured and simulated main sand front velocity versus time. The impact times for the flat bottom sample for each of the standoffs is indicated.

Figure 9. Simulation of sand particle progression towards the baseline test target for a standoff distance of 29 cm. The particle velocity is color coded. The position of the sensors used to monitor the particle position and velocity are indicated in (a).

Figure 10. Comparison of the strain gauge measured (black line) and simulated (red dashed line) pressure-time waveforms for the flat-bottomed target at standoff distances of (a) 19 cm, (c) 24 cm and (e) 29 cm. The impulse-time waveforms are also shown for each standoff distance and the arrival times of the 1^{st} and 2^{nd} distal reflection at the strain gauges are indicated on (b), (d), and (f). The time t = 0 s again corresponds to initiation of detonation of the Detasheet.

Figure 11. (a) Impulse at the first distal reflection (up to 558 μs after the signal first arrives at the strain gauge) for each of the three standoff distances for the flat (baseline) target, the solid V-block target, and the V-block target with the aluminum slider plates. (b) Impulse at the second reflection (748 μs after the first reflection) for each of the targets.

Figure 12. High-speed video image sequence of sand impact with the V-shaped target at a standoff distance of 29 cm. The target geometry is indicated by white lines in (d)-(f).

Figure 13. Simulation of sand impact with the V-shaped target for a standoff distance of 29 cm.

Figure 14. Comparison of the strain gauge measured (black line) and simulated (red dashed line) pressure-time waveforms for the V-shaped target at standoff distances of (a) 19 cm, (c) 24 cm and (e) 29 cm. (b), (d), and (f) Show the impulse-time waveforms are also shown for each standoff distance together with the arrival times of the 1st and 2nd distal reflections at the strain gauges. Time t = 0 s is the instant of detonation.

Figure 15. High-speed video image sequence for the V-shaped target with aluminum slider plates impacted by sand for a 29 cm standoff distance. The target geometry is indicated by white lines in (d)-(f).

Figure 16. Simulation time sequence of sand impacting V-shaped target with attached slider plates for 29 cm standoff distance.

Figure 17. Multiple exposure image of a sliding plate target test at a 29 cm standoff distance. The sliding plate (left) location at t = 370 ms after detonation is shown and its trajectory over time is indicated by the dotted line. The time for each slider plate position is shown (in milliseconds) at approximately 100 ms intervals.

Figure 18. High-speed video images of V-block target with aluminum slider plates at 19 cm standoff distance. (a) The test rig at t = 0 s (the moment of detonation), (b) t = 0.3 ms, (c) t = 1.2 ms, (d) t = 5.5 ms, (e) t = 35.6 ms, and (f) t = 48.2 ms. The two aluminum slider plates are visible as they were ejected from the target in (e) and (f). The white dotted lines show the approximate trajectory.

Figure 19. Sand particle propagation simulations for a V-block target with sliding plates showing the sliding plate movement after impact. The standoff distance was 19 cm. The dark red particles represent high explosive particles and the brown particles the wet sand.

Figure 20. Comparison of the strain gauge measured (black line) and simulated (red dashed line) pressure-time waveforms for the V-shaped target with aluminum slider plates at standoff distances of (a) 19 cm, (c) 24 cm and (e) 29 cm. The impulse-time waveforms for each standoff distance are shown in (b), (d), and (f) together with the arrival times of the 1st and 2nd distal reflections.

Figure 21. Impulse distributions on the bottom of the flat block, V-block target, and the V-block with slider plates at 2 ms after detonation for each standoff distance. The simulations used a coefficient of friction of 0.5 between the sand and roughened surface, and a value of 0.05 for the lubricated interface between the slider and target.

Figure 22. (a) Comparison of impulse transfer to the V-block target (solid lines) and the V-block target with aluminum sliding plates (dashed lines) for the three standoff distances. (b) The normalized plate sliding distance during sand impact.

Figure 23. (a) The total simulated transferred impulse after 4 ms in the Z direction to the test targets at the strain gauge location. (b) The contributions to the total simulated Z-impulse transferred to the test targets and the attachment plate.

Figure 24. Simulated impulse ratio in the Z direction versus sand velocity. The effect of changing the inclination angle from the flat bottom geometry to the V-block using a friction coefficient of 0.5 and zero is indicated. The ratio for the impulse transferred by only the sand particles indicates a contribution of gaseous particles to the total transferred impulse. The impulse ratio for a sliding plate geometry in the resolved frictionless limit for $\alpha = 53°$ is also shown.

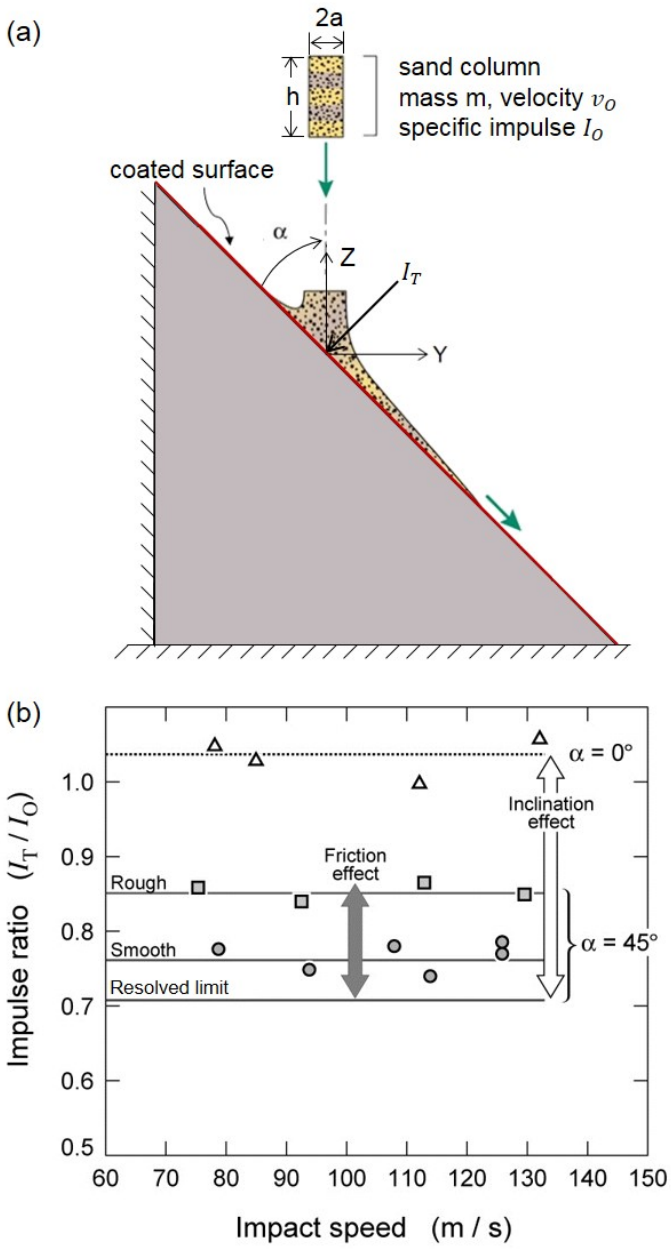

Figure 1. (a) A schematic illustration of the impact of a sand column of length h and momentum mv_o with an inclined coated surface. The transmitted impulse to the structure, I_T, is balanced by a reaction momentum for a rigidly clamped (or massive) target. (b) The measured effect of target surface inclination and roughness upon the fraction of the incident momentum transferred to the target. The fraction of the incident momentum resolved onto the frictionless α = 45° plane is also shown as the resolved limit. (Modified from reference 20)

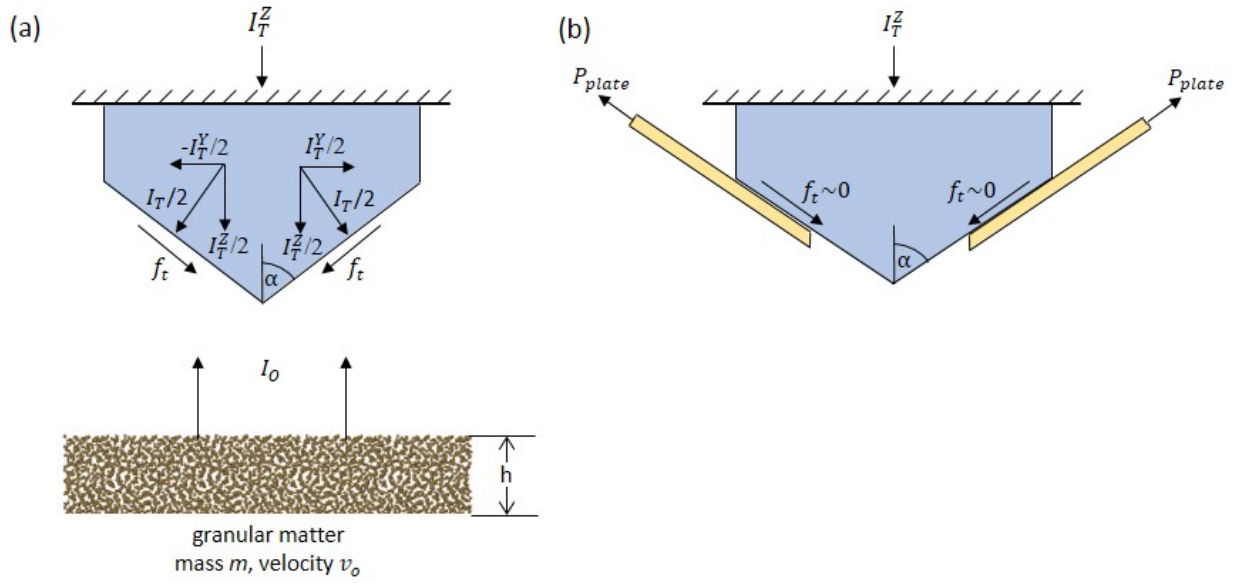

Figure 2. Reaction momenta during impact of a granular matter slab of thickness h with (a) a V-block target and (b) a V-shaped target with a pair of sliding plates attached.

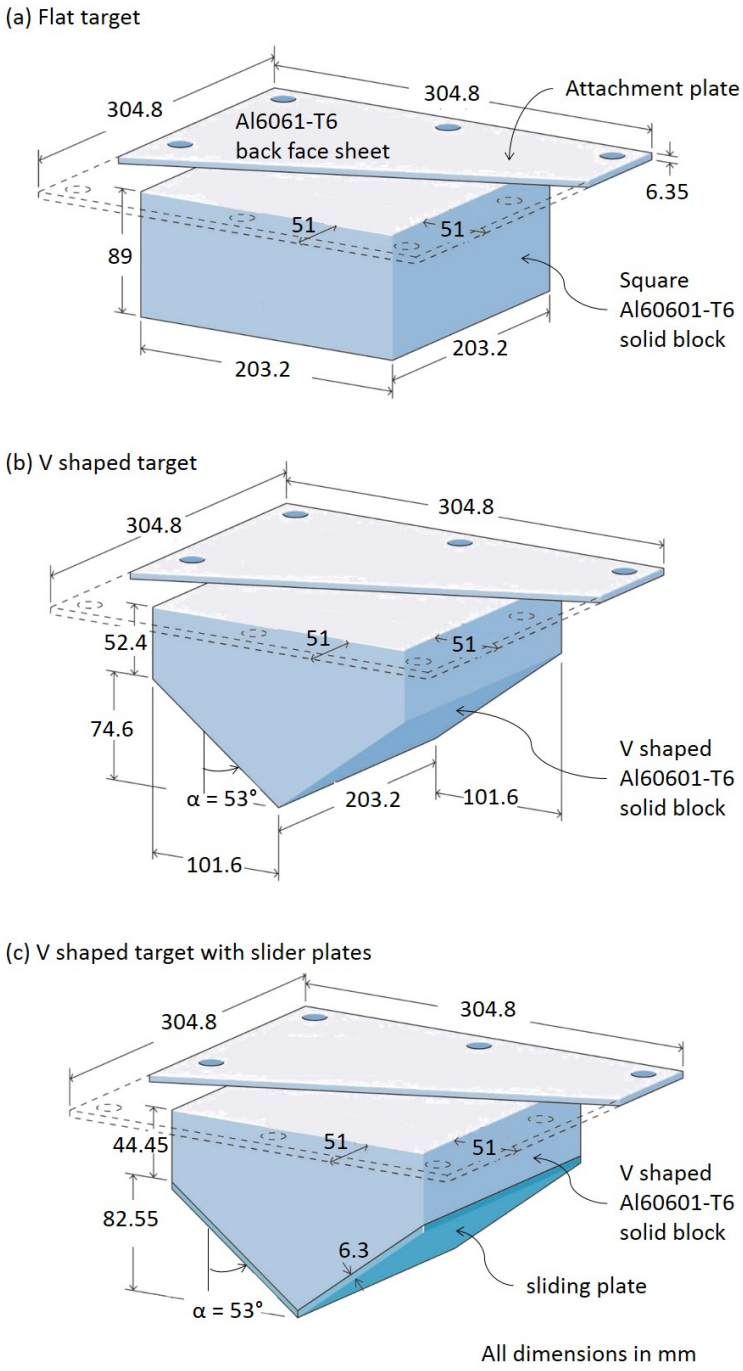

Figure 3. The three Al 6061-T6 targets used for the impulse transfer study: (a) The flat bottom target, (b) the V-shaped target with surfaces inclined at 53^{o} to the incident sand and (c) the V-shaped target with a pair of sliding plates attached.

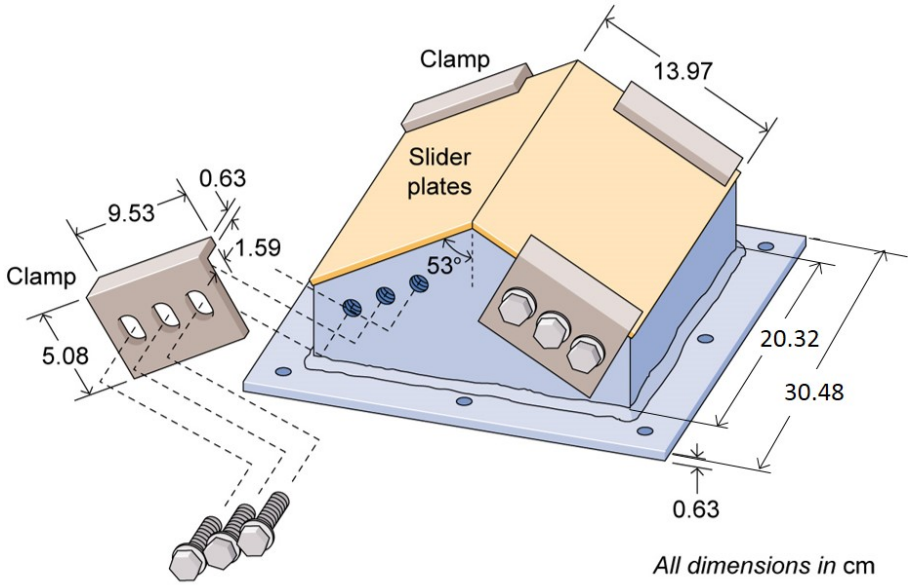

Figure 4. The sliding plate target geometry showing the use of four edge clamps that act as guides for the sliding plates during sand impact.

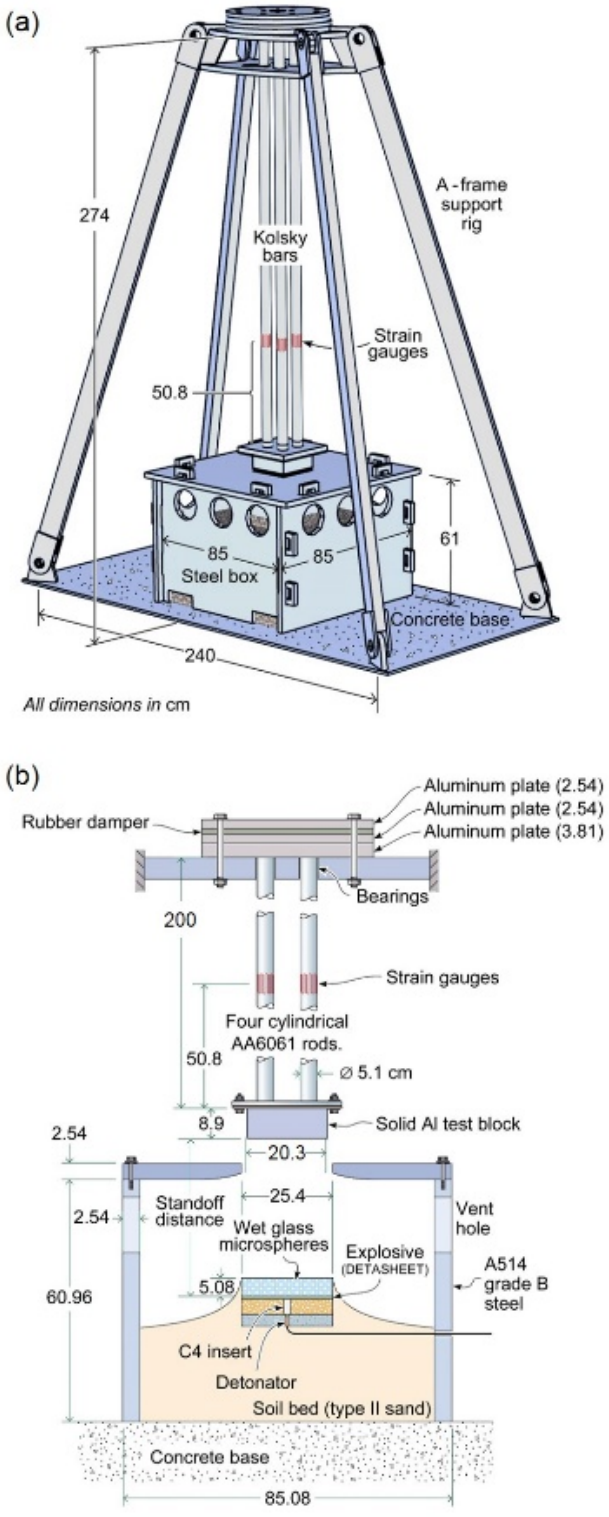

Figure 5. (a) Schematic illustration of the vertical impulse test rig with a flat-bottomed solid aluminum target attached. (b) An expanded view of the interior of the steel box, the test charge design, the sample location, and the strain gauge location on the Kolsky bars.

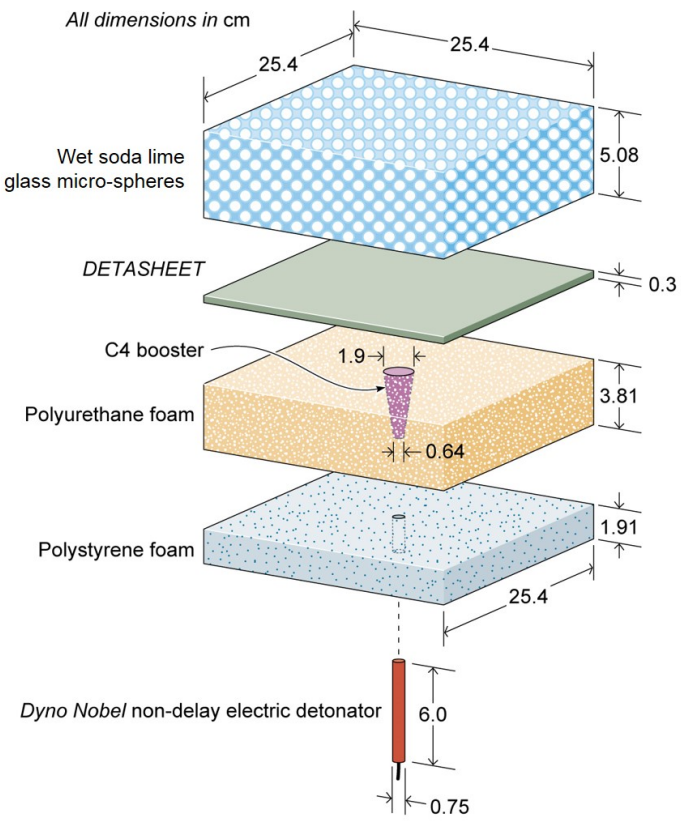

Figure 6. Schematic illustration of the test charge geometry.

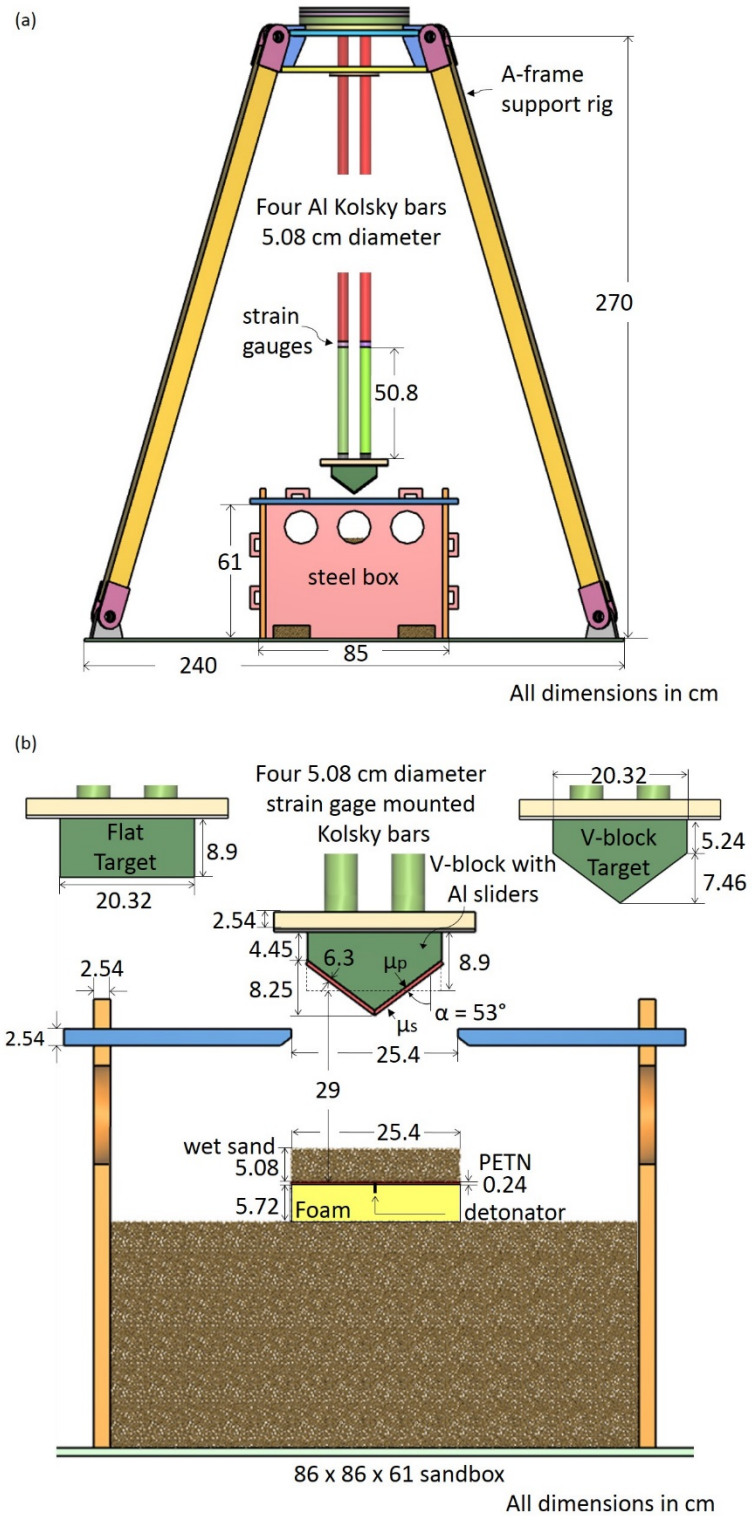

Figure 7. (a) The FE model of the vertical impulse test rig. Each color-coded part used a different model and material combination. (b) The simulation geometry within the sandbox. The V-block target with sliding plates is shown for a standoff distance of 29 cm. The model geometries of the flat block and V-block targets are also shown.

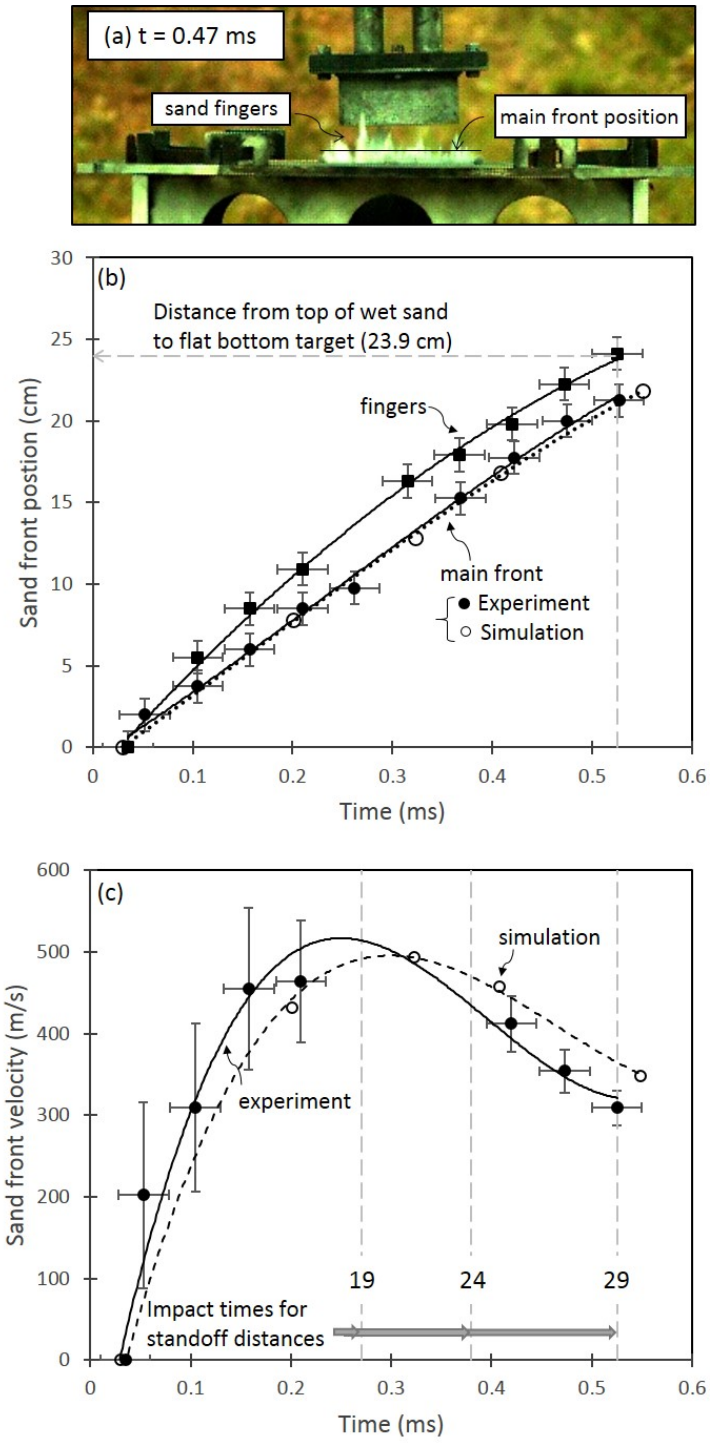

Figure 8. (a) A photograph of the sand front at 0.47 ms after detonation showing the main front position and the presence of sand fingers for a test with the flat bottom sample at a standoff distance of 29 cm. (b) The measured and simulated main sand front position versus time and measured fingers position versus time. (c) The measured and simulated main sand front velocity versus time with the impact times for the flat bottom sample atr each of the standoff distances.

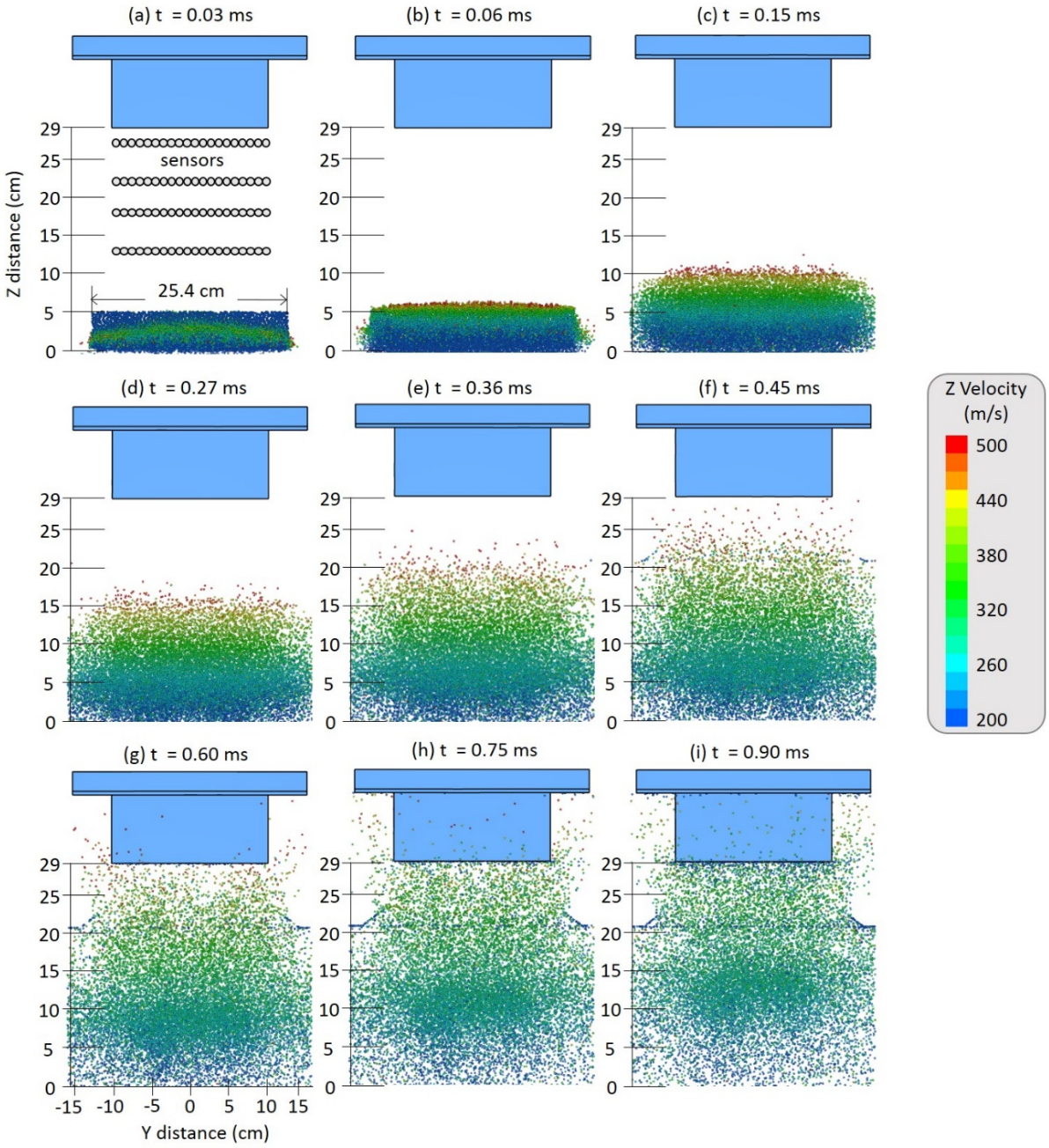

Figure 9. Simulation of sand particle progression towards the baseline test target for a standoff distance of 29 cm. The particle velocity is color coded. The position of the sensors used to monitor the particle position and velocity are indicated in (a).

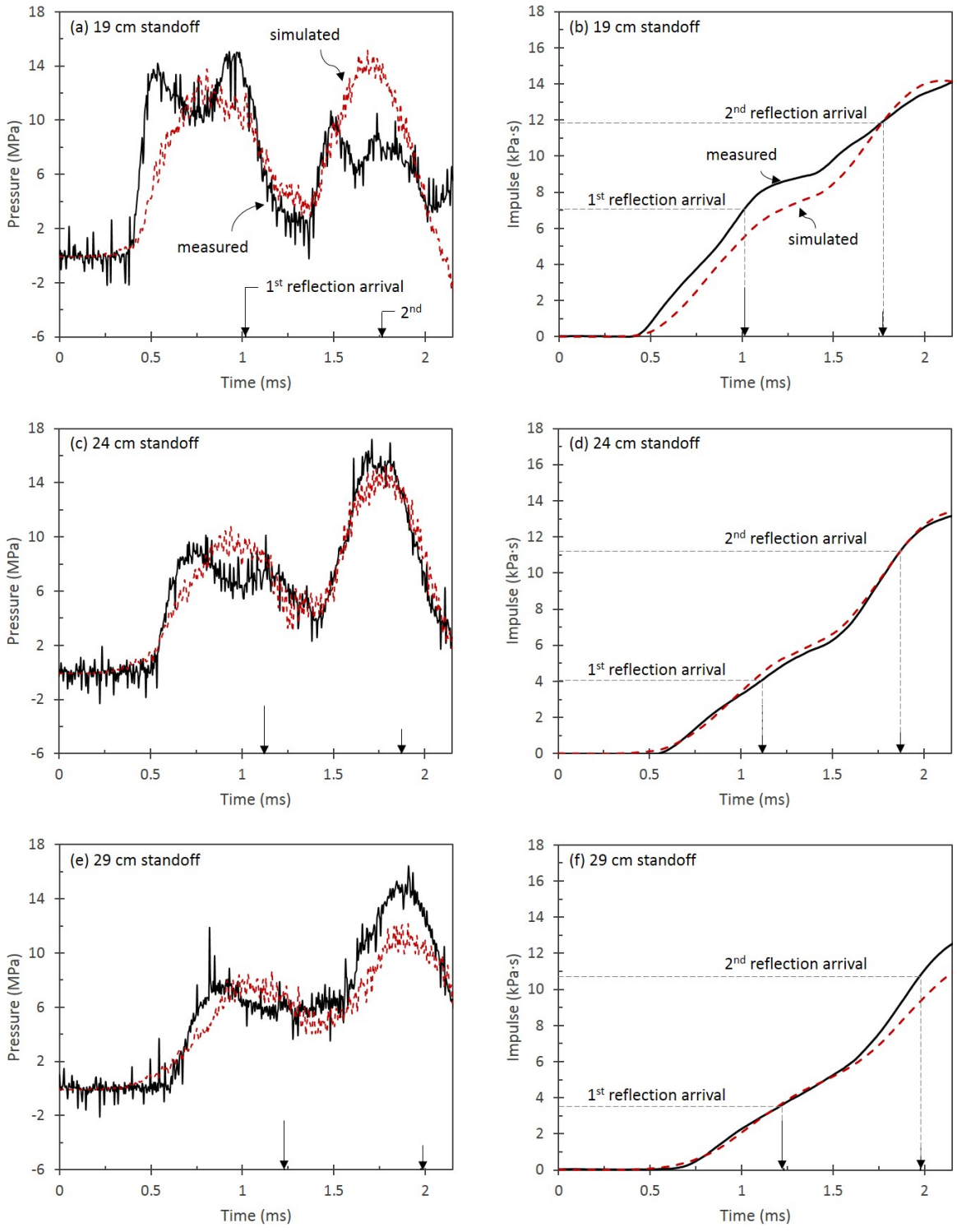

Figure 10. Comparison of the strain gauge measured (black line) and simulated (red dashed line) pressure-time waveforms for the flat-bottomed target at standoff distances of (a) 19 cm, (c) 24 cm and (e) 29 cm. The impulse-time waveforms are also shown for each standoff distance and the arrival times of the 1st and 2nd distal reflection at the strain gauges are indicated on (b), (d), and (f). The time t = 0 s again corresponds to initiation of detonation of the Detasheet.

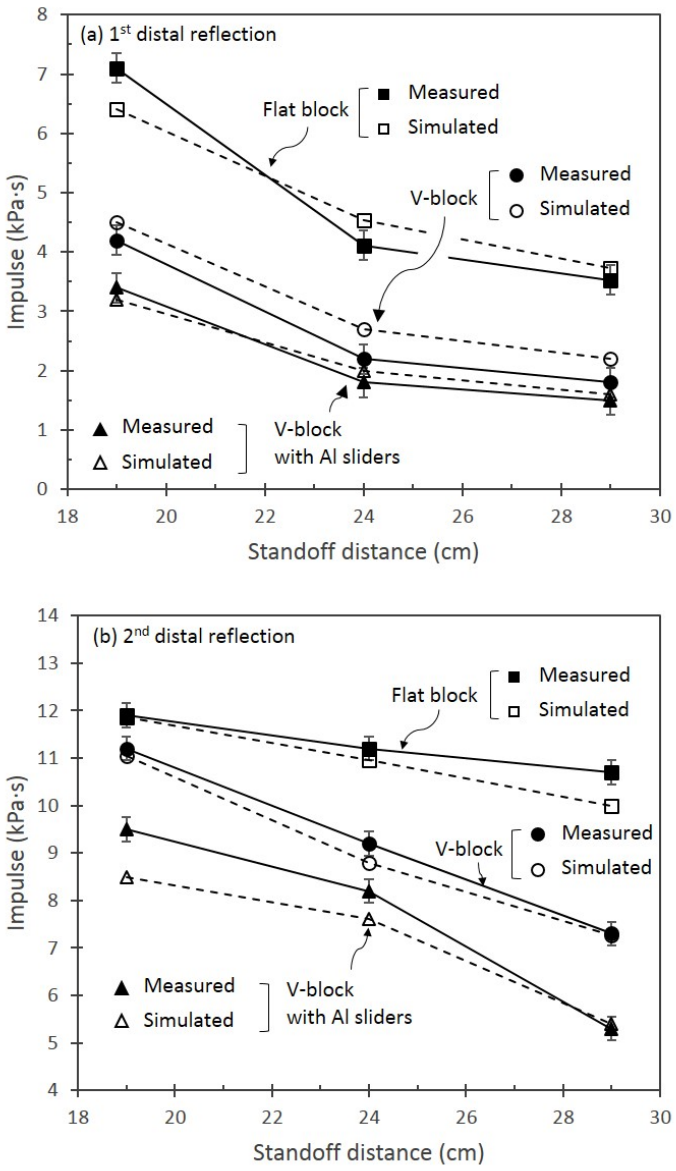

Figure 11. (a) Impulse at the first distal reflection (up to 558 μs after the signal first arrives at the strain gauge) for each of the three standoff distances for the flat bottomed (baseline) target, the V-block target, and the V-block target with the aluminum slider plates. (b) Impulse at the second reflection (748 μs after the first reflection) for each of the targets.

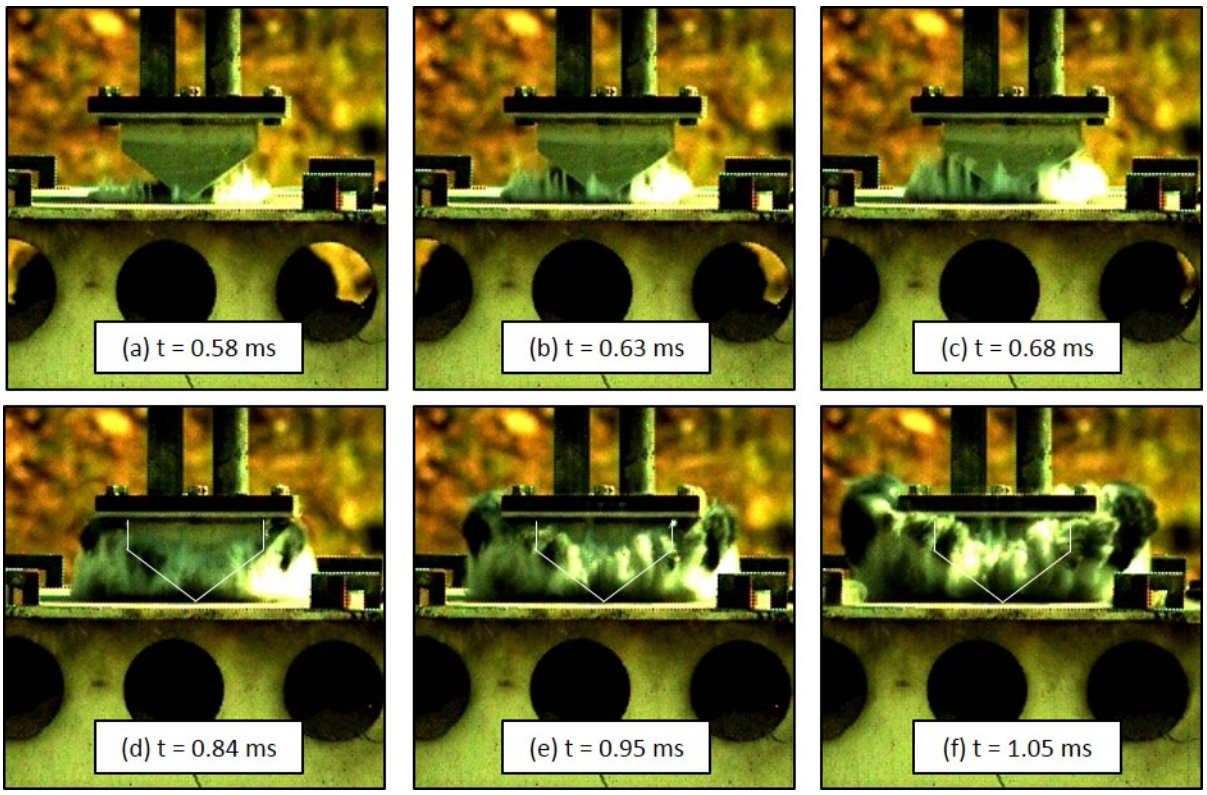

Figure 12. High-speed video image sequence of sand impact with the V-shaped target at a standoff distance of 29 cm. The (obscured) target position is indicated by white lines in (d)-(f).

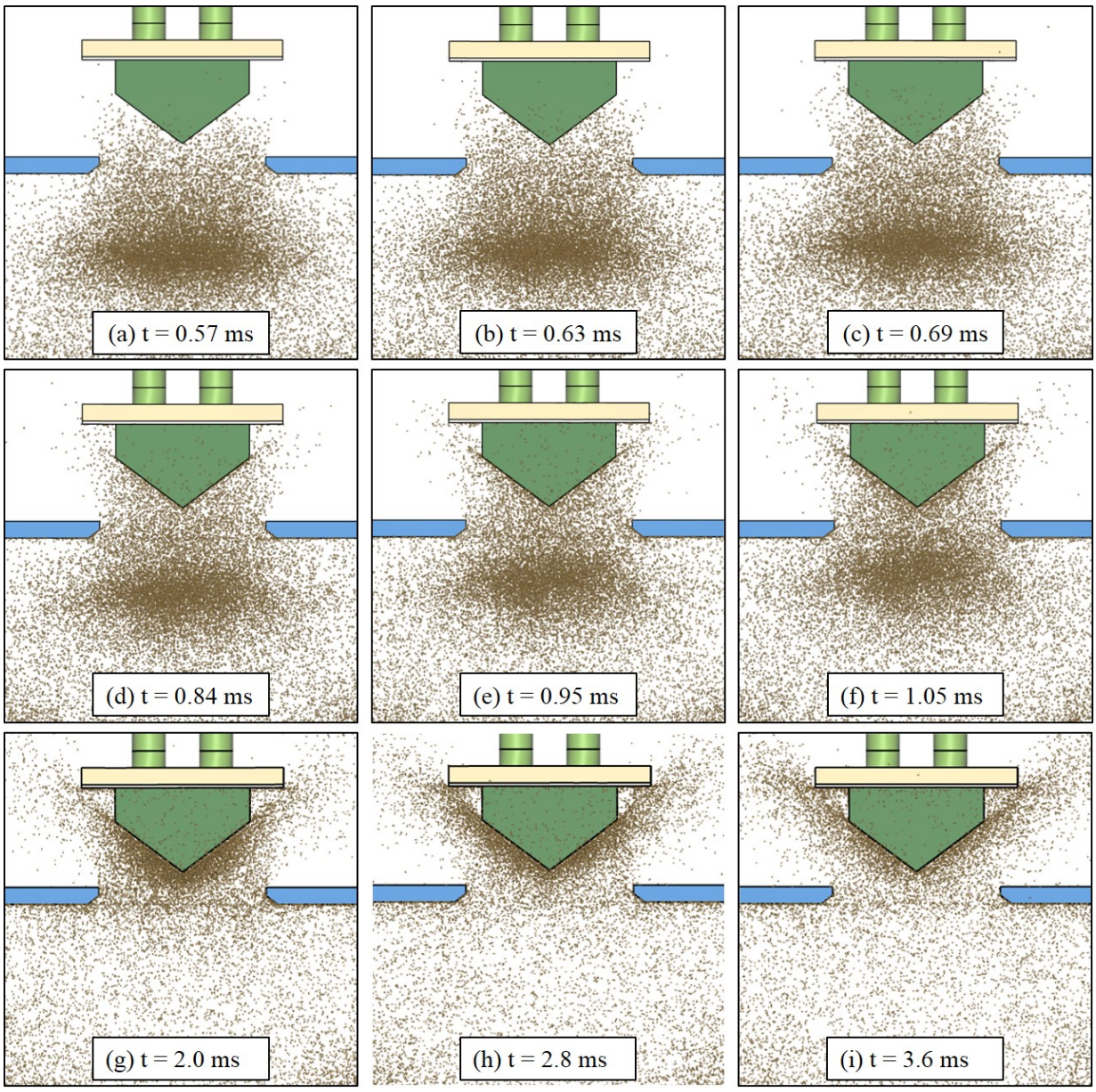

Figure 13. Simulation of sand impact with the V-shaped target for a standoff distance of 29 cm.

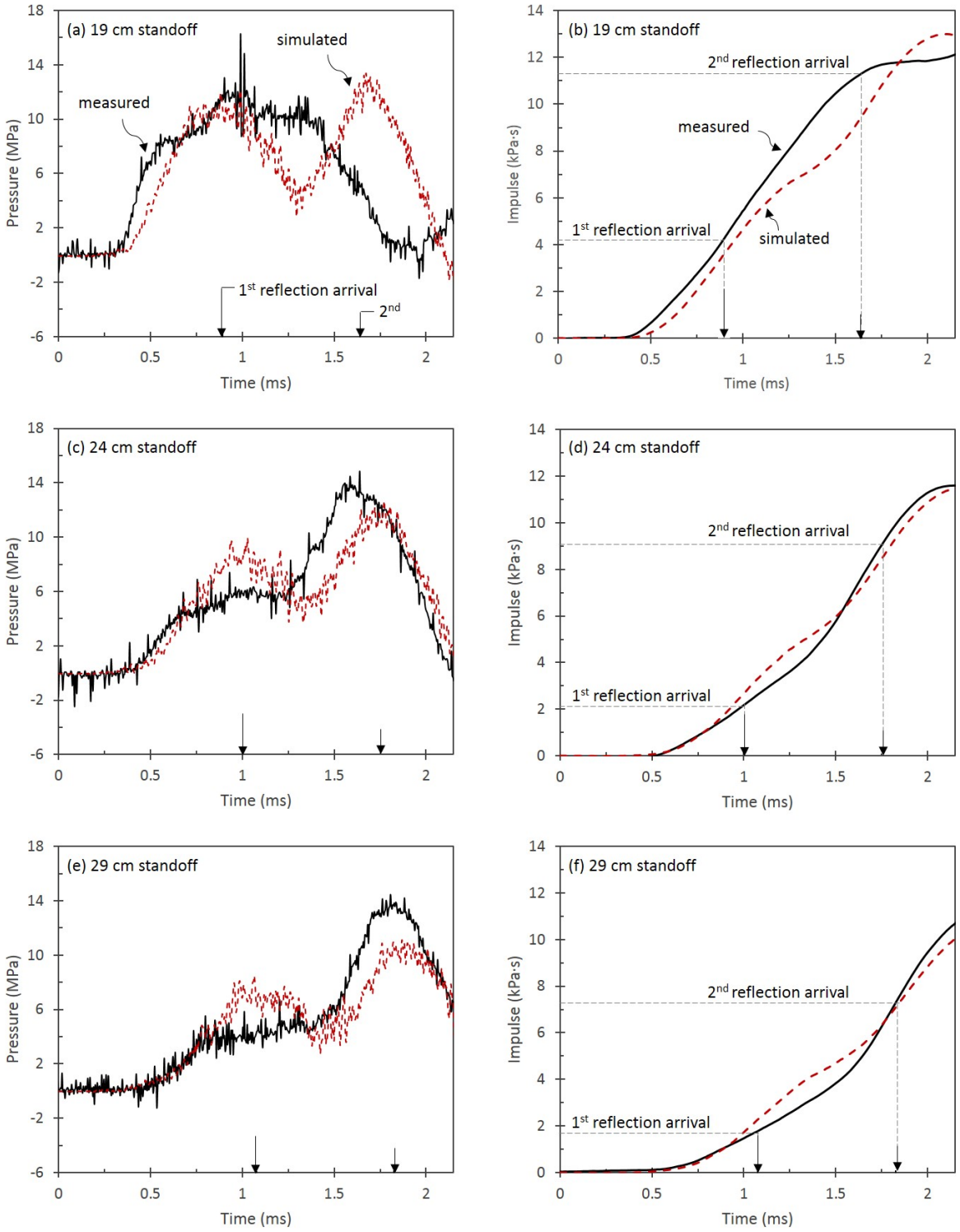

Figure 14. Comparison of the strain gauge measured (black line) and simulated (red dashed line) pressure-time waveforms for the V-shaped target at standoff distances of (a) 19 cm, (c) 24 cm and (e) 29 cm. Figures (b), (d), and (f) show the impulse-time waveforms for each standoff distance together with the arrival times of the 1st and 2nd distal reflections at the strain gauges. Time t = 0 s corresponds to the instant of detonation.

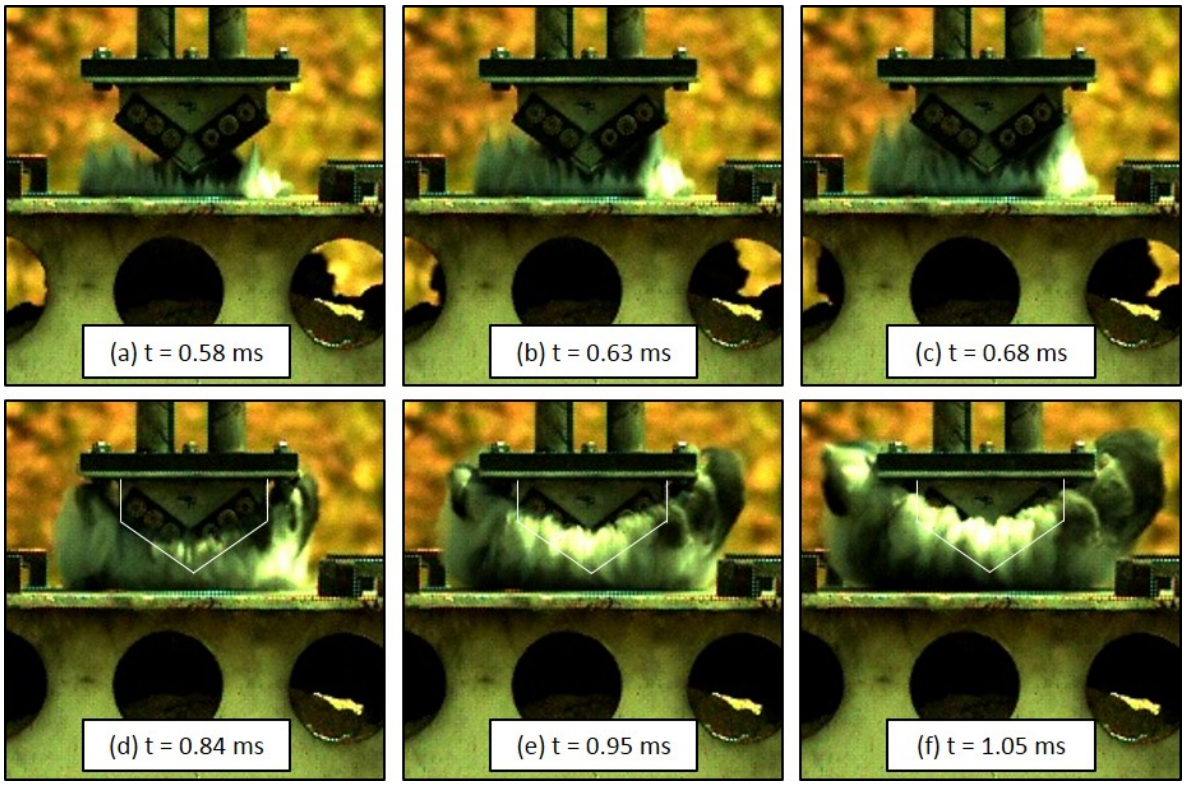

Figure 15. High-speed video image sequence for the V-shaped target with aluminum slider plates impacted by sand for a 29 cm standoff distance. The target geometry is indicated by white lines in (d)-(f).

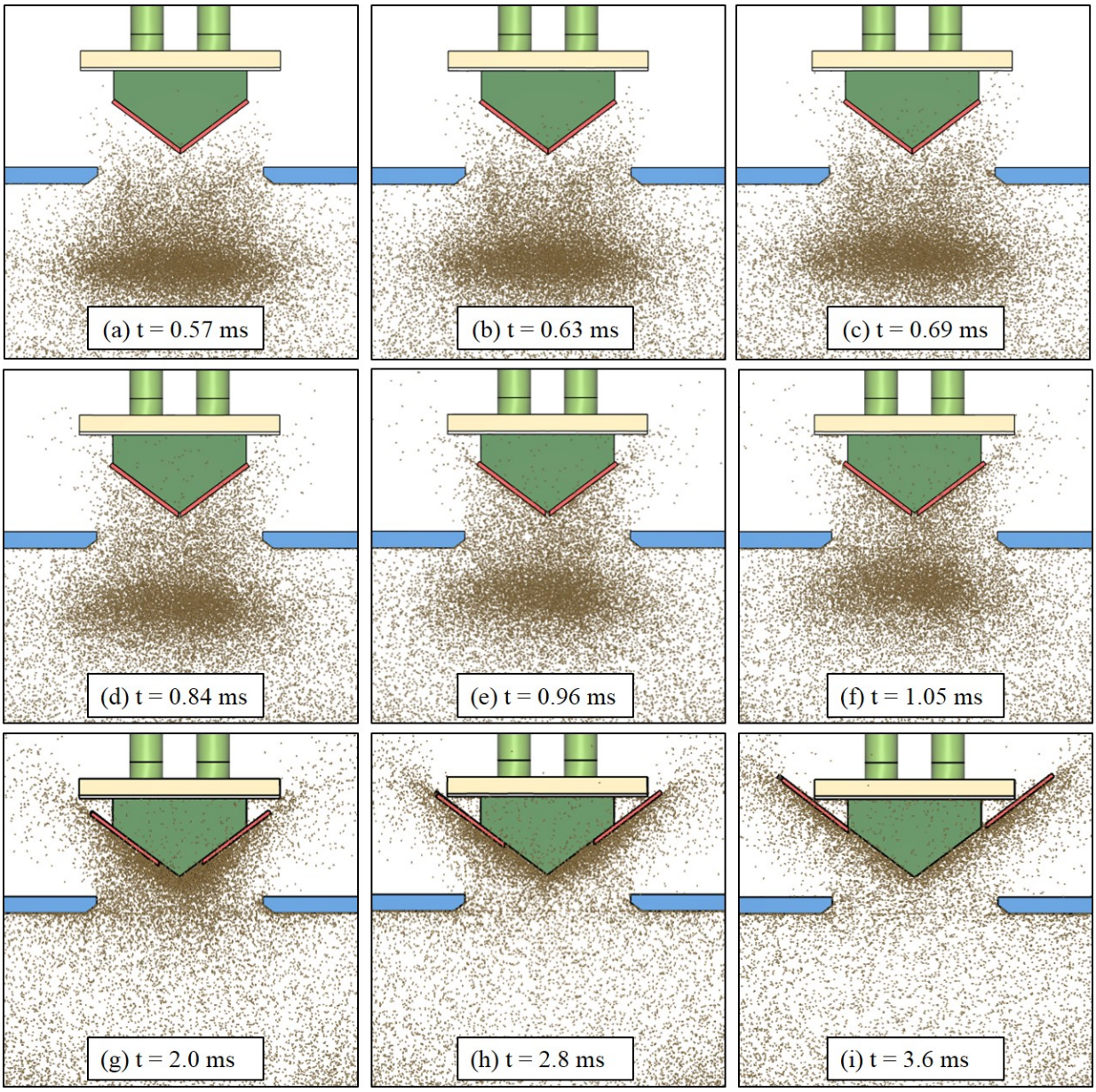

Figure 16. Simulation time sequence of sand impact with the V-shaped target with attached slider plates for 29 cm standoff distance.

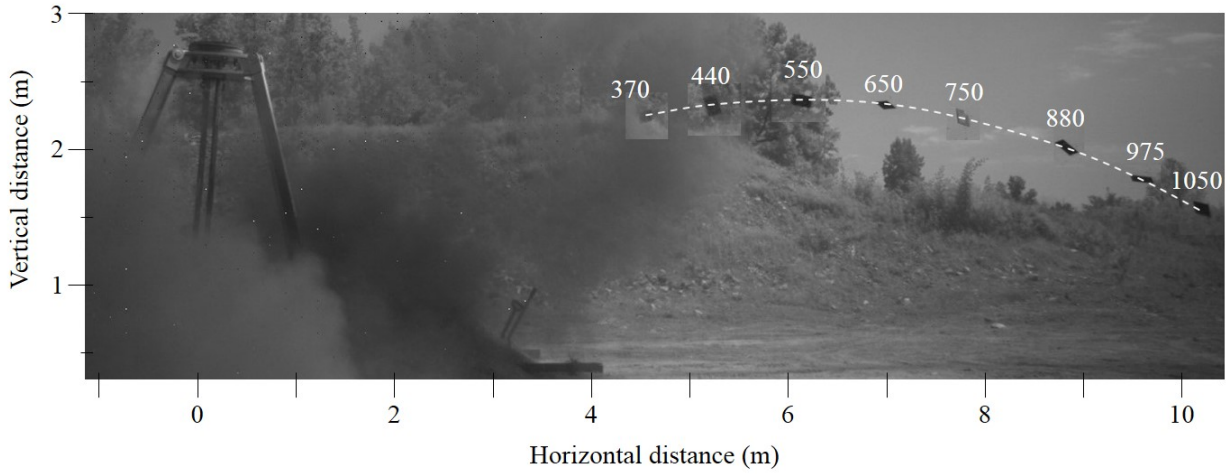

Figure 17. Multiple exposure image of a sliding plate target test at a 29 cm standoff distance. The sliding plate (left) location at t = 370 ms after detonation is shown and its trajectory over time is indicated by the dotted line. The time for each slider plate position is shown (in milliseconds) at approximately 100 ms intervals.

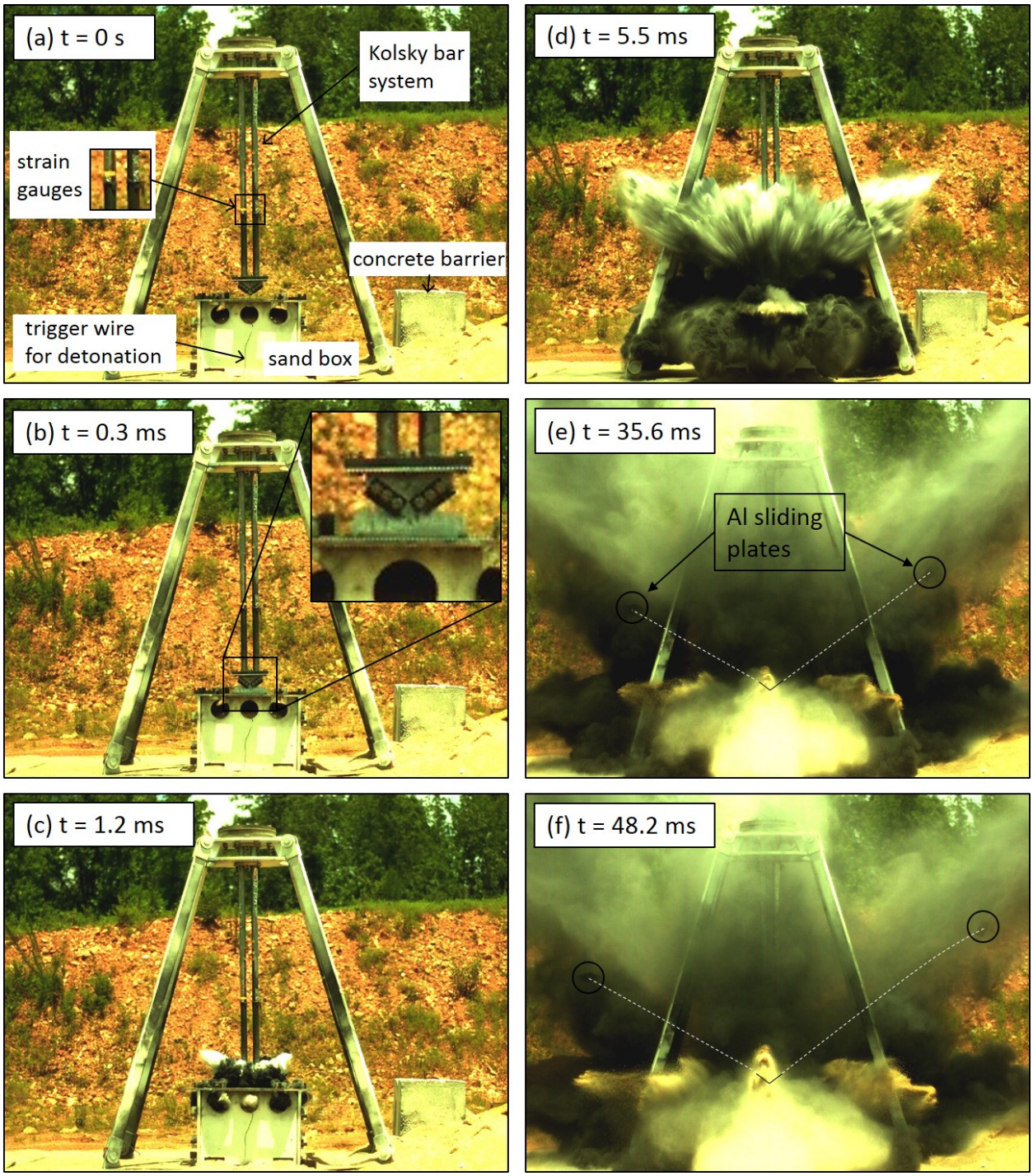

Figure 18. High-speed video images of V-block target with aluminum slider plates at 19 cm standoff distance. (a) The test rig at t = 0 s (the moment of detonation), (b) t = 0.3 ms, (c) t = 1.2 ms, (d) t = 5.5 ms, (e) t = 35.6 ms, and (f) t = 48.2 ms. The two aluminum slider plates are visible as they were ejected from the target in (e) and (f). The white dotted lines show the approximate trajectory.

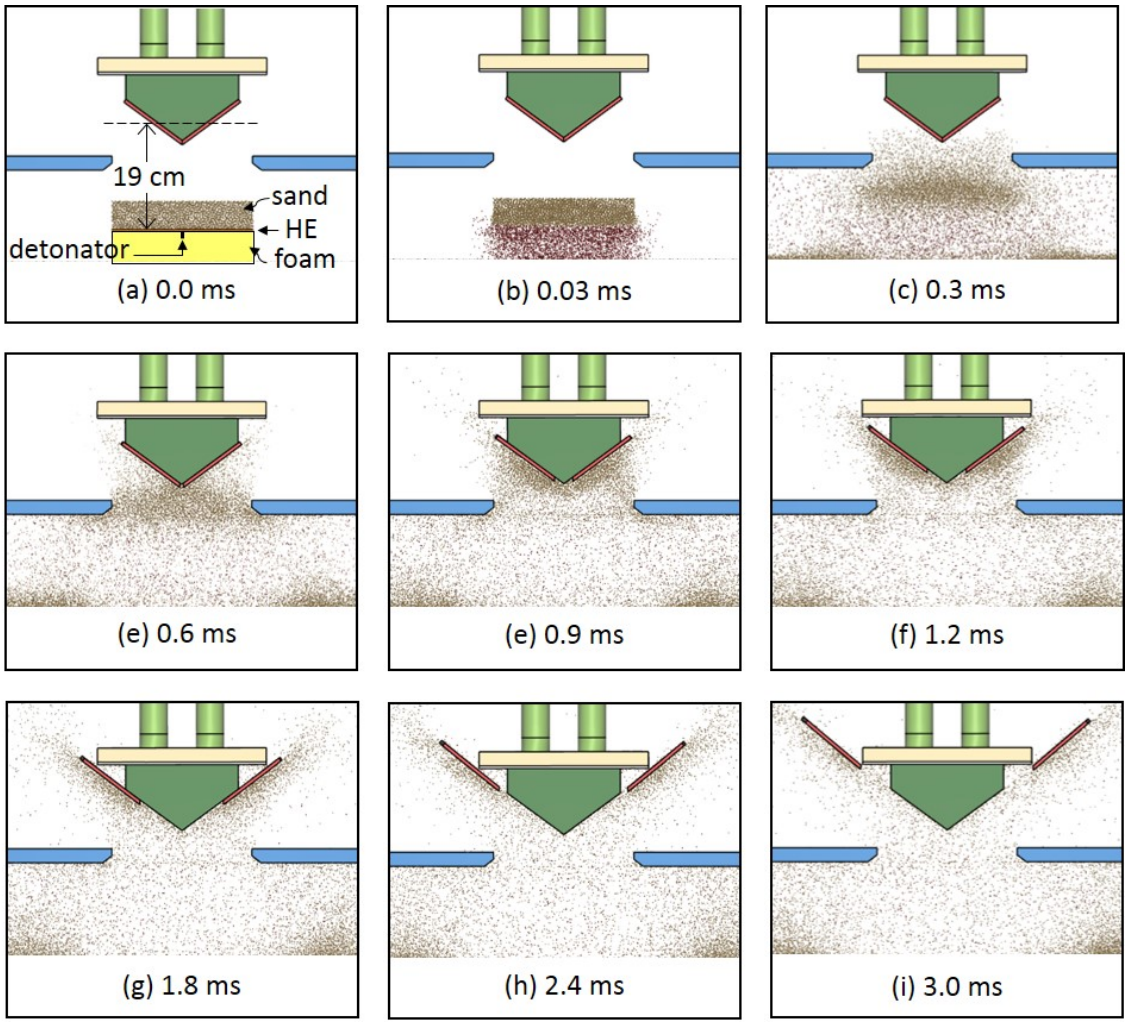

Figure 19. Sand particle propagation simulations for a V-block target with sliding plates showing the sliding plate movement after impact. The standoff distance was 19 cm. The dark red particles represent high explosive particles and the brown particles the wet sand.

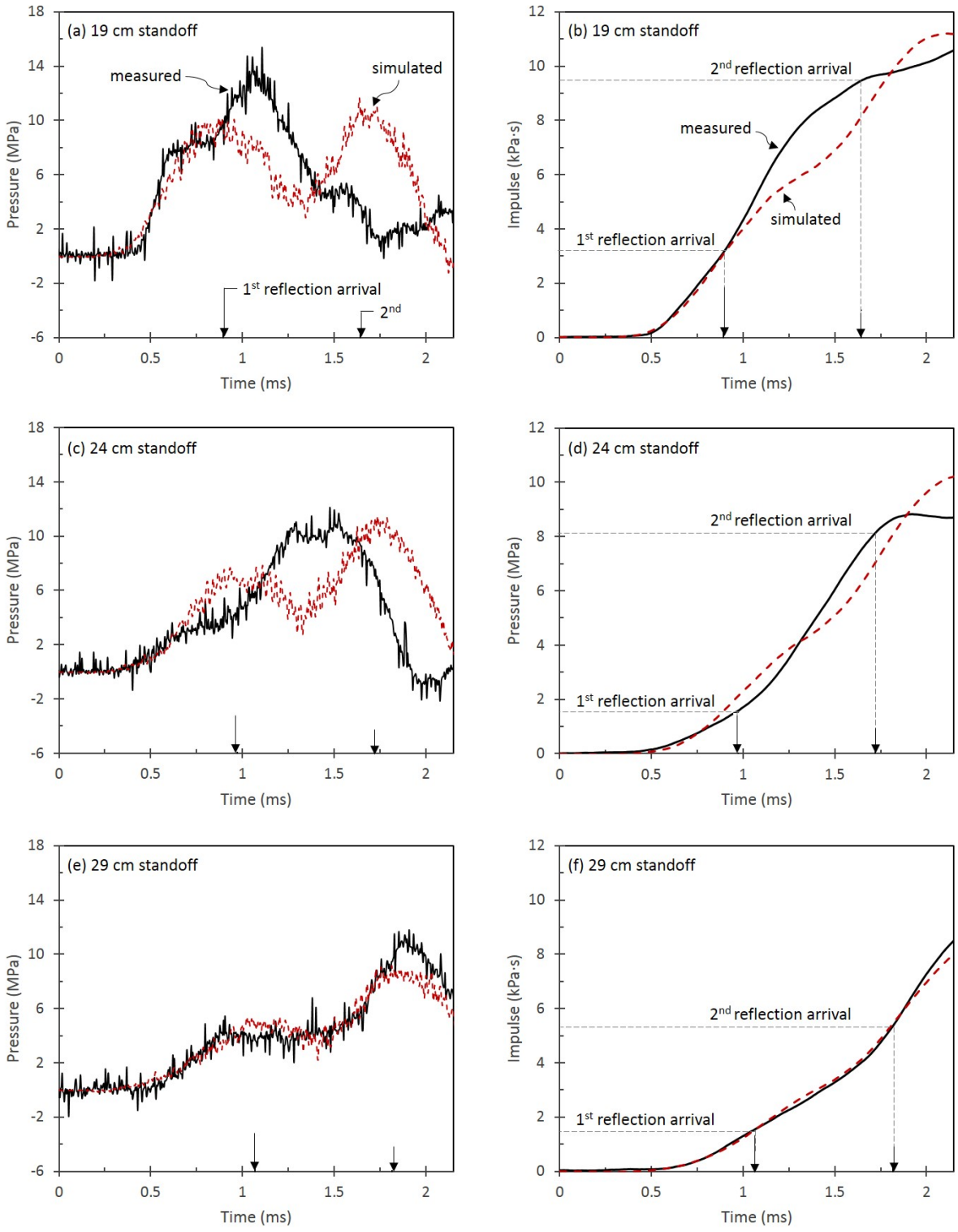

Figure 20. Comparison of the strain gauge measured (black line) and simulated (red dashed line) pressure-time waveforms for the V-shaped target with aluminum slider plates at standoff distances of (a) 19 cm, (c) 24 cm and (e) 29 cm. The impulse-time waveforms for each standoff distance are shown in (b), (d), and (f) together with the arrival times of the 1st and 2nd distal reflections.

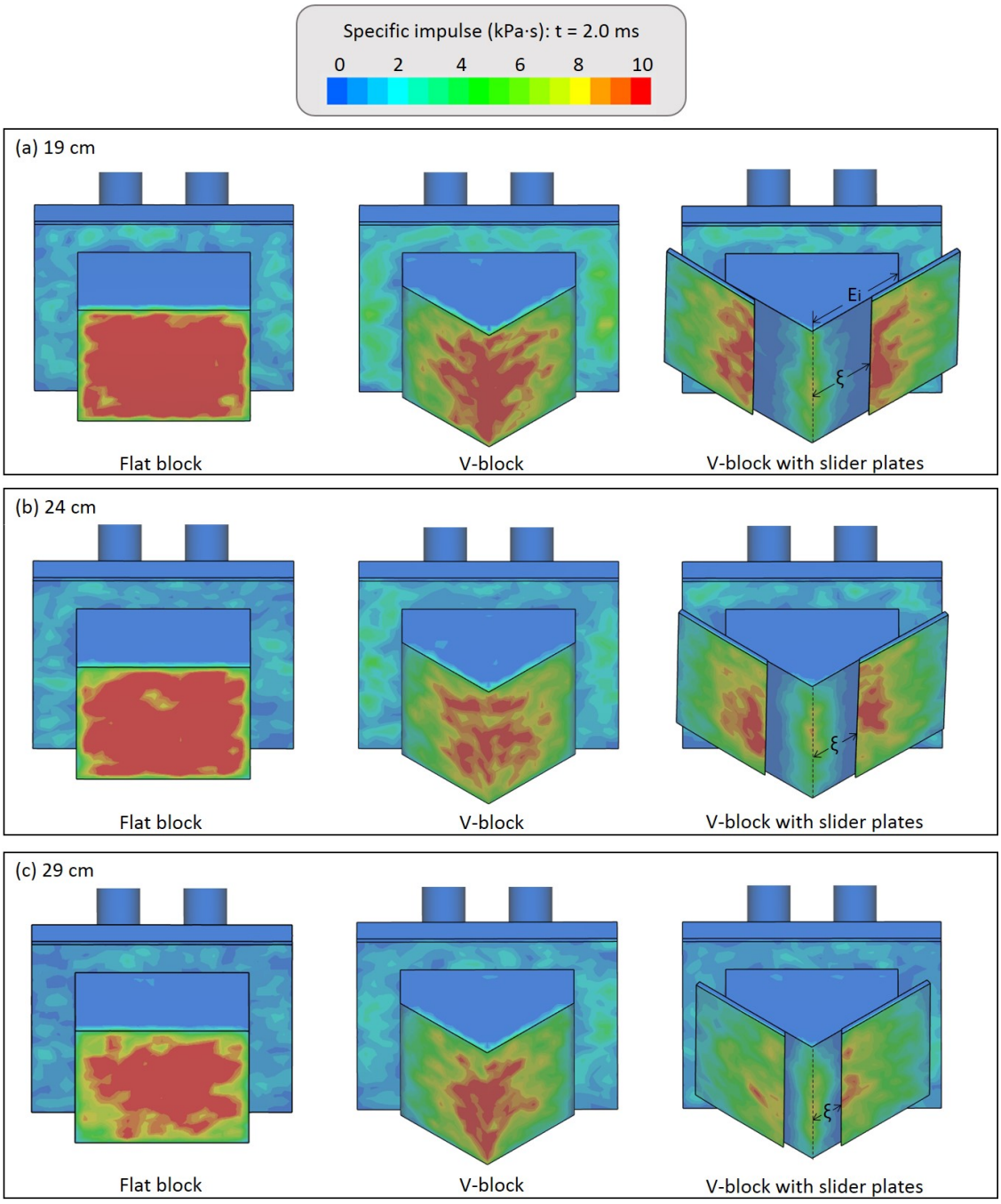

Figure 21. Impulse distributions on the bottom of the flat block, V-block target, and the V-block with slider plates accumulated during the first 2 ms after detonation for each standoff distance. The simulations used a coefficient of friction μ_s=0.5 between the sand and roughened target surface, and a friction value of 0.05 for the lubricated interface between the slider and target.

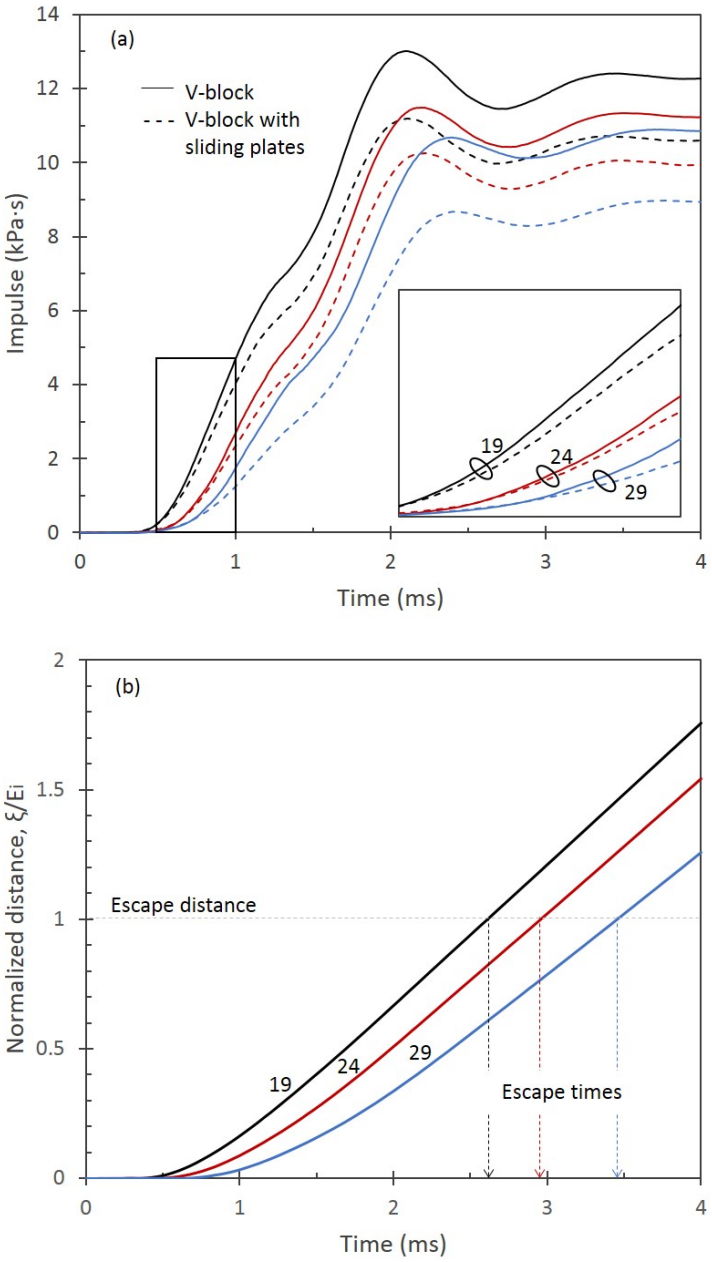

Figure 22. (a) Comparison of impulse transfer to the V-block target (solid lines) and the V-block target with aluminum sliding plates (dashed lines) for the three standoff distances. (b) The normalized plate sliding distance versus time during sand impact for the three standoff distances. The distance and time of sliding for plate escape from the V-block are also shown for each standoff distance.

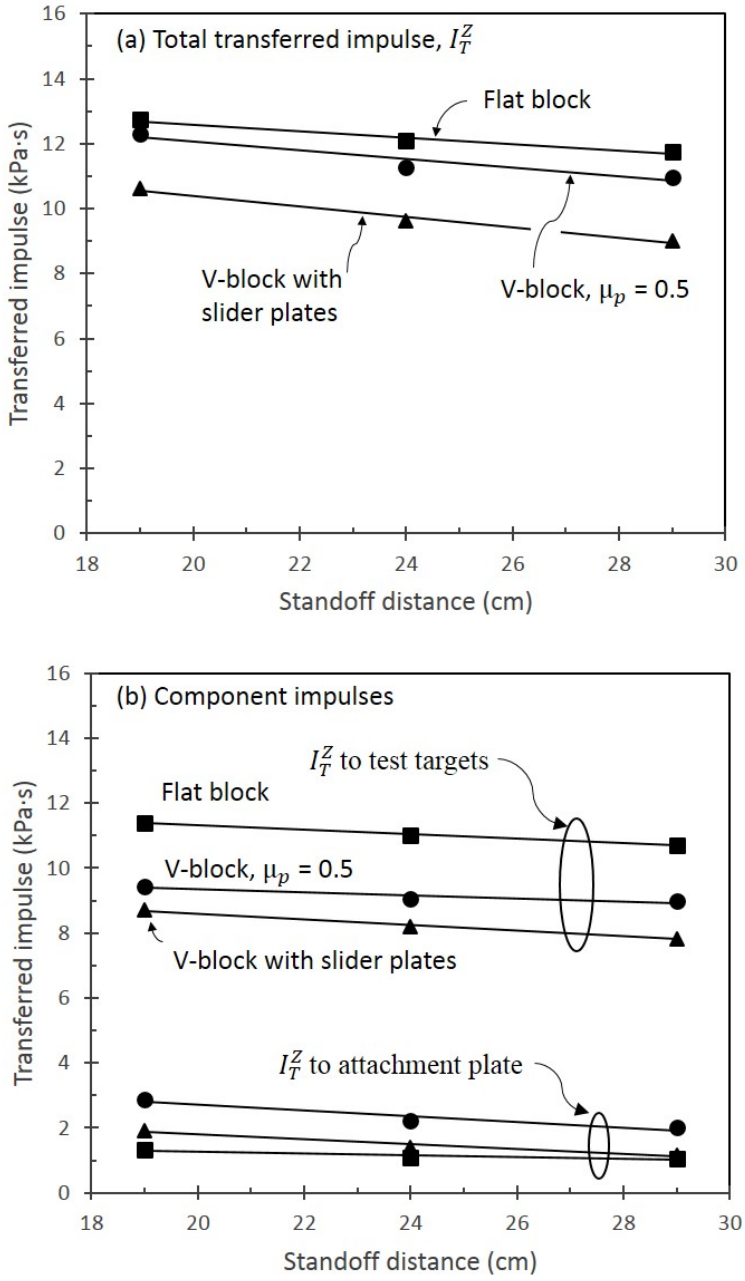

Figure 23. (a) The total simulated transferred impulse in the Z-direction after 4 ms calculated at the strain gauge location. (b) The impulse contributions transferred to the test targets and to the periphery of their attachment plate.

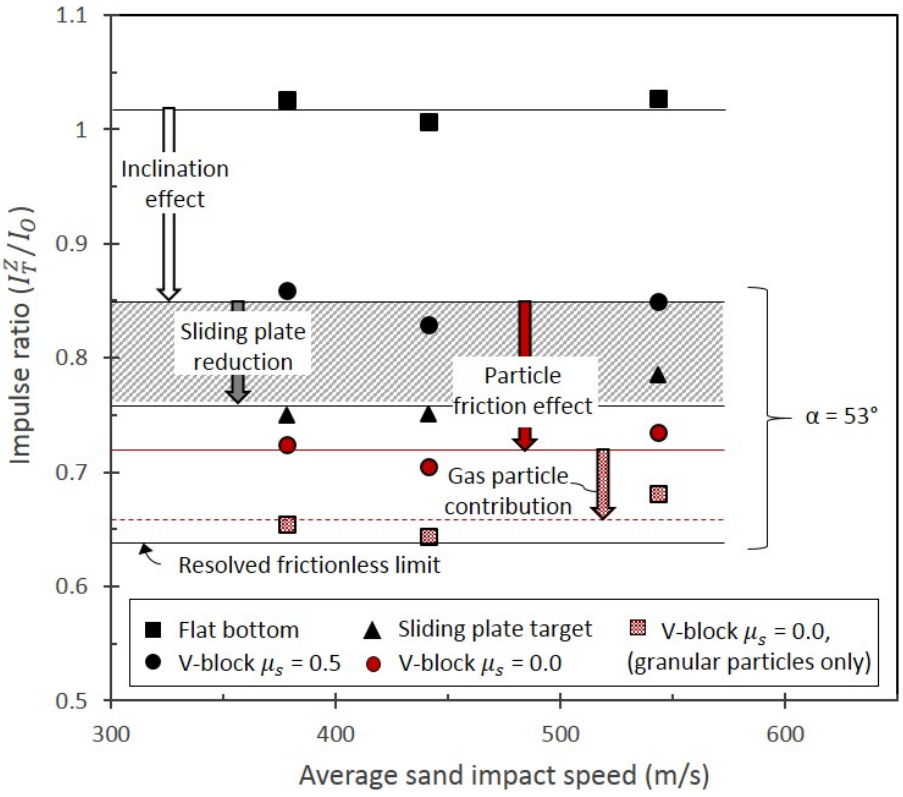

Figure 24. The simulated transferred impulse ratio in the Z-direction versus average sand particle velocity. The impulse of the (flat-bottomed) target with $\alpha = 0^o$ dropped from 1.02 to 0.85 when $\alpha = 53°$ and a particle-target friction coefficient μ_s=0.5 was used. The effect of the frictional interaction between sand particles and the inclined plate can be seen by comparing the μ_s=0.5 and 0.0 results. This resulted in a decrease in impulse ratio from 0.85 to 0.72. The use of a sliding plate reduced the impulse ratio from 0.85 to 0.76. A fraction of the impulse was transferred to the targets by air and detonation product particles with no frictional interaction. When their contribution was subtracted from the results, the impulse transferred by frictionless sand particles approached the $\alpha = 53^o$ resolved frictionless limit.

Can you use open and filled symbols so they can be resolved in B and W?